Cell Metabolism

Article

Exosomal miR-302b rejuvenates aging mice by reversing the proliferative arrest of senescent cells

Graphical abstract

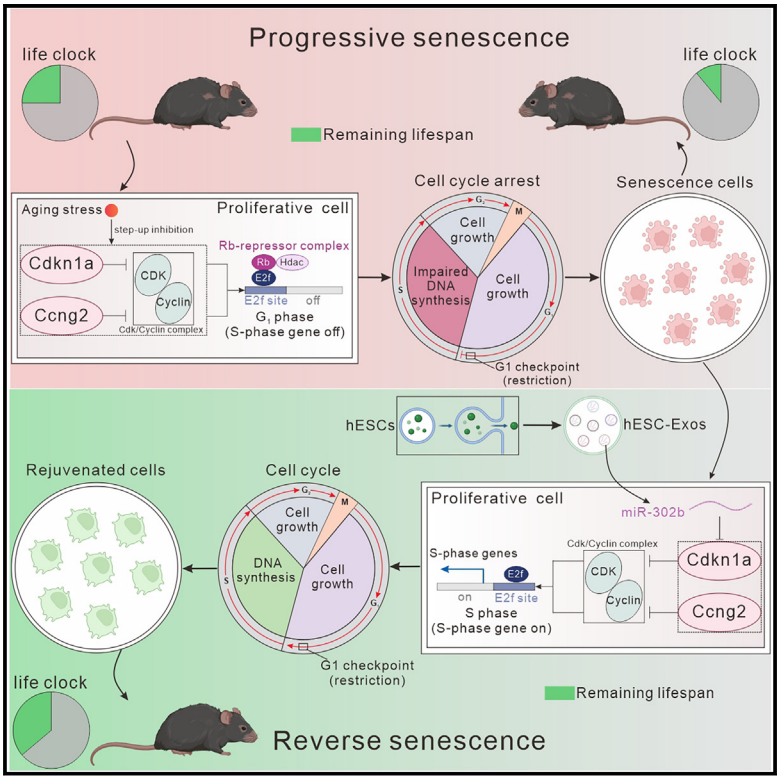

Highlights

- miR-302b in hESC-Exos targets *Cdkn1a*/*Ccng2*, reversing proliferative arrest in SnCs
- miR-302b extends lifespan and improves physical ability and cognition in aging mice
- Long-term miR-302b delivery shows no increased disease or tumor burden during 24 months
- Senoreverse strategy reverses proliferative arrest in SnCs, achieving rejuvenation

Authors

Youkun Bi, Xinlong Qiao, Zhaokui Cai, ..., Hongjin Wu, Yuanchao Xue, Guangju Ji

Correspondence

baoo766@shutcm.edu.cn (H.W.), ycxue@ibp.ac.cn (Y.X.), gj28@ibp.ac.cn (G.J.)

In brief

Bi et al. propose the Senoreverse anti-aging strategy, which aims to reverse the proliferative arrest of senescent cells. Exosomal miR-302b is identified as a Senoreverse candidate that targets the cell cycle inhibitors *Cdkn1a* and *Ccng2*, rejuvenating aging mice by improving physical and cognitive functions, extending lifespan, and exhibiting no safety concerns throughout a 24-month observation period.

Bi et al., 2025, Cell Metabolism *37*, 527–541
February 4, 2025
https://doi.org/10.1016/j.cmet.2024.11.013

CellPress

Cell Metabolism

CellPress
OPEN ACCESS

Article

Exosomal miR-302b rejuvenates aging mice by reversing the proliferative arrest of senescent cells

Youkun Bi,[1,2,6] Xinlong Qiao,[3,6] Zhaokui Cai,[2] Hailian Zhao,[2] Rong Ye,[2] Qun Liu,[2] Lin Gao,[3] Yingqi Liu,[3] Bo Liang,[1] Yixuan Liu,[1] Yaning Zhang,[1] Zhiguang Yang,[3] Yanyun Wu,[2] Huiwen Wang,[1,2] Wei Jia,[4] Changqing Zeng,[1] Ce Jia,[2] Hongjin Wu,[5,*] Yuanchao Xue,[1,2,*] and Guangju Ji[1,2,7,*]

[1]Henan Academy of Sciences, Zhengzhou 450000, China
[2]Institute of Biophysics, Chinese Academy of Sciences, Beijing 100101, China
[3]Yuan Sheng Biotechnology Ltd., Qingdao 266109, China
[4]Biomedical Institute of TaishengKangyuan Ltd., Beijing 100103, China
[5]Boao International Hospital, Shanghai University of Traditional Chinese Medicine, Hainan 571434, China
[6]These authors contributed equally
[7]Lead contact
*Correspondence: baoo766@shutcm.edu.cn (H.W.), ycxue@ibp.ac.cn (Y.X.), gj28@ibp.ac.cn (G.J.)
https://doi.org/10.1016/j.cmet.2024.11.013

SUMMARY

Cellular senescence, a hallmark of aging, involves a stable exit from the cell cycle. Senescent cells (SnCs) are closely associated with aging and aging-related disorders, making them potential targets for anti-aging interventions. In this study, we demonstrated that human embryonic stem cell-derived exosomes (hESC-Exos) reversed senescence by restoring the proliferative capacity of SnCs *in vitro*. In aging mice, hESC-Exos treatment remodeled the proliferative landscape of SnCs, leading to rejuvenation, as evidenced by extended lifespan, improved physical performance, and reduced aging markers. Ago2 Clip-seq analysis identified miR-302b enriched in hESC-Exos that specifically targeted the cell cycle inhibitors *Cdkn1a* and *Ccng2*. Furthermore, miR-302b treatment reversed the proliferative arrest of SnCs *in vivo*, resulting in rejuvenation without safety concerns over a 24-month observation period. These findings demonstrate that exosomal miR-302b has the potential to reverse cellular senescence, offering a promising approach to mitigate senescence-related pathologies and aging.

INTRODUCTION

Aging is an intrinsic biological process characterized by systemic alterations that progressively compromise physiological integrity and increase susceptibility to age-related maladies, ultimately culminating in mortality.[1,2] The hallmarks of aging include cellular senescence, genomic instability, epigenetic alterations, loss of proteostasis, stem cell exhaustion, chronic inflammation, and altered intercellular communication.[1,3] Of these, cellular senescence is a state of stable cell cycle arrest triggered by various stressors and an important driver of aging.[4–7] Senescent cells (SnCs) accumulate during aging and secrete the senescence-associated secretory phenotype (SASP), promoting secondary senescence and disrupting normal tissue functions.[3,5,7,8] Consequently, targeting SnCs has emerged as a promising strategy to prolong healthspan and delay the onset of age-related diseases.[7,9]

Therapies targeting SnCs are broadly divided into two major categories: elimination of SnCs (senolytic) and suppression of pathological SASP signaling (senomorphic).[10,11] These strategies have shown therapeutic benefits in aging and related diseases, including extending lifespan, alleviating inflammation, and improving cognition.[12] However, they also have certain limitations.[8,9] While the senolytic strategy may effectively eliminate SnCs when scarce, the prevalence of SnCs in tissues increases as individuals age.[8,13] Eliminating them may result in considerable tissue damage and compromise normal organ function.[8,9] Moreover, although SASP suppression has rejuvenating effects, it can impede immune surveillance of pathogens and cancer cells.[7,9] Developing new rejuvenation strategies that target SnCs is crucial to address these challenges.

Although cellular senescence is generally considered irreversible, emerging studies suggest that senescence in specific cell types can be dynamic, allowing SnCs to re-enter the cell cycle and resume normal functioning.[9,14] However, the potential contribution of reversing the proliferative arrest of SnC to rejuvenate aging remains unexplored. Additionally, mounting evidence has highlighted that human embryonic stem cell-derived exosomes (hESC-Exos) have regenerative and rejuvenating effects in local tissues, such as the hippocampus and bone marrow.[15–17] Previous research indicates that hESC-Exos contain numerous loaded proteins and microRNAs (miRNAs)

that are predicted to regulate aging and proliferation.[15] Therefore, we present a new rejuvenation strategy called Senoreverse, which aims to reverse the proliferative arrest of SnCs and achieve rejuvenation. Targeting SnCs using hESC-Exos treatment is a potentially feasible approach within the Senoreverse strategy.

RESULTS

hESC-Exos rejuvenated senescent IMR-90 cells

We first tested whether hESC-Exos treatment could reverse the senescent phenotypes and rejuvenate SnCs. Purified hESC-Exos were prepared using the density gradient centrifugation method and identified (Figures S1A–S1C).[18,19] Normal human diploid fibroblast strains undergo senescence after multiple divisions.[4,20] The human fibroblast cell line IMR-90 exhibits a youthful state when it reaches the population doubling level (PDL) at 30 but undergoes complete senescence at PDL50.[21] We treated the PDL50 IMR-90 cells with hESC-Exos for 72 h (Figure 1A) and observed significant rescue of senescence phenotypes. This was evidenced by decreased senescence-associated β-galactosidase (SA-β-gal) activity (Figures 1B and 1C), downregulated expression of senescence- and SASP-related genes (*CDKN2A*, *CDKN1A*, *IL-1a*, *IL-11*, and *CCL20*) (Figures 1D–1F), promoted cell proliferation in a population doubling assay (Figure 1G), increased cell proliferation marker Ki67 expression (Figures 1H and 1I), and an elevated proportion of cells in the S phase (Figures 1J and 1K).

Next, we performed RNA sequencing (RNA-seq) to characterize the effects of hESC-Exos on the proliferation-related gene expression profiles of PDL50 IMR-90 cells (Table S1). Our findings indicate that hESC-Exos significantly repressed the expression of known senescence-related genes, such as *TP53*, *IL-6*, *CDKN1A*, and *CDKN2A*,[1] while enhancing the expression of proliferation-related genes, including *MKI67*, *PCNA*, *TOP2A*, and *CDK1* (Figure 1L).[22–24] Additionally, the upregulated differentially expressed genes (DEGs) were commonly associated with cellular senescence and inflammatory responses, whereas downregulated DEGs were commonly associated with the mitotic cell cycle and cell cycle phase transition (Figure 1M). Gene set enrichment analysis (GSEA)[23] revealed that hESC-Exos treatment enhanced cell cycle enrichment (Figure 1N). These findings suggest that hESC-Exos treatment rejuvenated senescent IMR-90 cells and remodeled their proliferative potential.

hESC-Exos reversed the proliferative arrest of SnCs at single-cell resolution

To visually investigate the effect of hESC-Exos treatment on the proliferation of single SnCs, we generated a senescence reporter cell line by inserting the yellow fluorescent protein (YFP) gene downstream of the *CDKN1A* (code p21) stop codon and subsequently transfecting LO2 cells ("p21-YFP LO2 cells," Figure 2A). Temporal fluctuations in p21 expression were visualized using YFP signals. Doxorubicin (Dox) treatment was used to induce senescence in p21-YFP LO2 cells (Figure S1D). We used flow cytometry (FCM) to sort YFP-positive cells, identifying each in a state of senescence (Figure 2B), and subjected them to hESC-Exos or PBS treatment. The hESC-Exos treatment repressed the enhanced YFP signal and SA-β-gal activity induced by Dox while elevating the diminished expression of the proliferative marker Ki67 compared with PBS (Figures 2C and S1E). The live-cell workstation showed that hESC-Exos enabled the re-entry of some SnCs into the proliferative process (Video S1). By contrast, SnCs remained quiescent, accompanied by a progressively increasing YFP signal, with no signs of proliferation when treated with PBS (Video S2).

To observe the effects of hESC-Exos on transcriptional profiles associated with proliferation, we performed single-cell RNA-seq (scRNA-seq) on SnCs sorted by FCM and treated them with hESC-Exos or PBS. After quality control,[25] we captured 16,741 single-cell transcriptomes: 6,311 in Dox-PBS and 10,430 in Dox-Exos. Cell cycle progression was analyzed by plotting the average expression of G1/S vs. G2/M genes in each cell cluster, revealing a complete cell cycle trajectory. Cells were ranked based on their cell cycle progression, and Dox-Exos outperformed Dox-PBS in terms of the proportion of S-phase cells, with an increase of approximately 17% (Figures 2D and 2E; Table S2).

We then annotated the cell clusters according to previously reported proliferation and senescence markers,[26] defining cells with abundant expression of *MKI67* and *PCNA* as rejuvenated cells (Rej), those with abundant expression of *CDNK1A* and *TP53* as SnCs (Sen), and others as cells in an intermediate state (Int). Heatmap analysis revealed three cell types with high expression of specific gene clusters: *S100P*, *CDKN1A*, and *CDKN3* in Sen and *PCNA*, *MKI67*, and *MCM5* in Rej (Figure S1F). Dox-PBS and Dox-Exos cells exhibited high levels of senescence (*CDNK1A* and *TP53*) and proliferation (*MKI67* and *PCNA*) markers (Figure S1G). An inspection of uniform manifold approximation and projection (UMAP) visualizations showed that Dox-Exos had an augmented proportion of Rej cells and a simultaneously reduced proportion of Sen cells compared with Dox-PBS (Figures 2F and 2G).

Next, we identified DEGs along the pseudotemporal trajectories transitioning from Int to Sen and Int to Rej. Genes in module 1 represented those upregulated during Int-to-Rej differentiation, including *CENPF*, *SERBP1*, and *TOP2A*, which were enriched during mitosis. Module 2 contained genes that were upregulated during the differentiation of Int to Sen, such as *CCNG2*, *CDKN1C*, and *CDKN2A*, which participated in the regulation of cell senescence and SASP (Figure S1H; Table S2). Furthermore, the epithelial-to-mesenchymal transition (EMT) can partially counteract senescence.[27] To address this variable, we analyzed the expression of representative EMT markers and found no evidence of EMT activation (Figure S1I). Taken together, hESC-Exos treatment reversed the proliferative arrest of single SnCs, enabling them to regain their proliferative capacity.

hESC-Exos treatment rejuvenated aging mice

The rejuvenating effect of hESC-Exos was evaluated in mice (Figure 3A). Prior to that, we first confirmed the safety of hESC-Exos owing to the tumorigenicity of their parental cells, human embryonic cells (Figures S2A–S2C).[14,15] *In vivo* testing revealed that hESC-Exos treatment extended both the median and maximum lifespans of aging-Exos mice compared with those of aging-PBS control mice (Figure 3B). Morphologically,

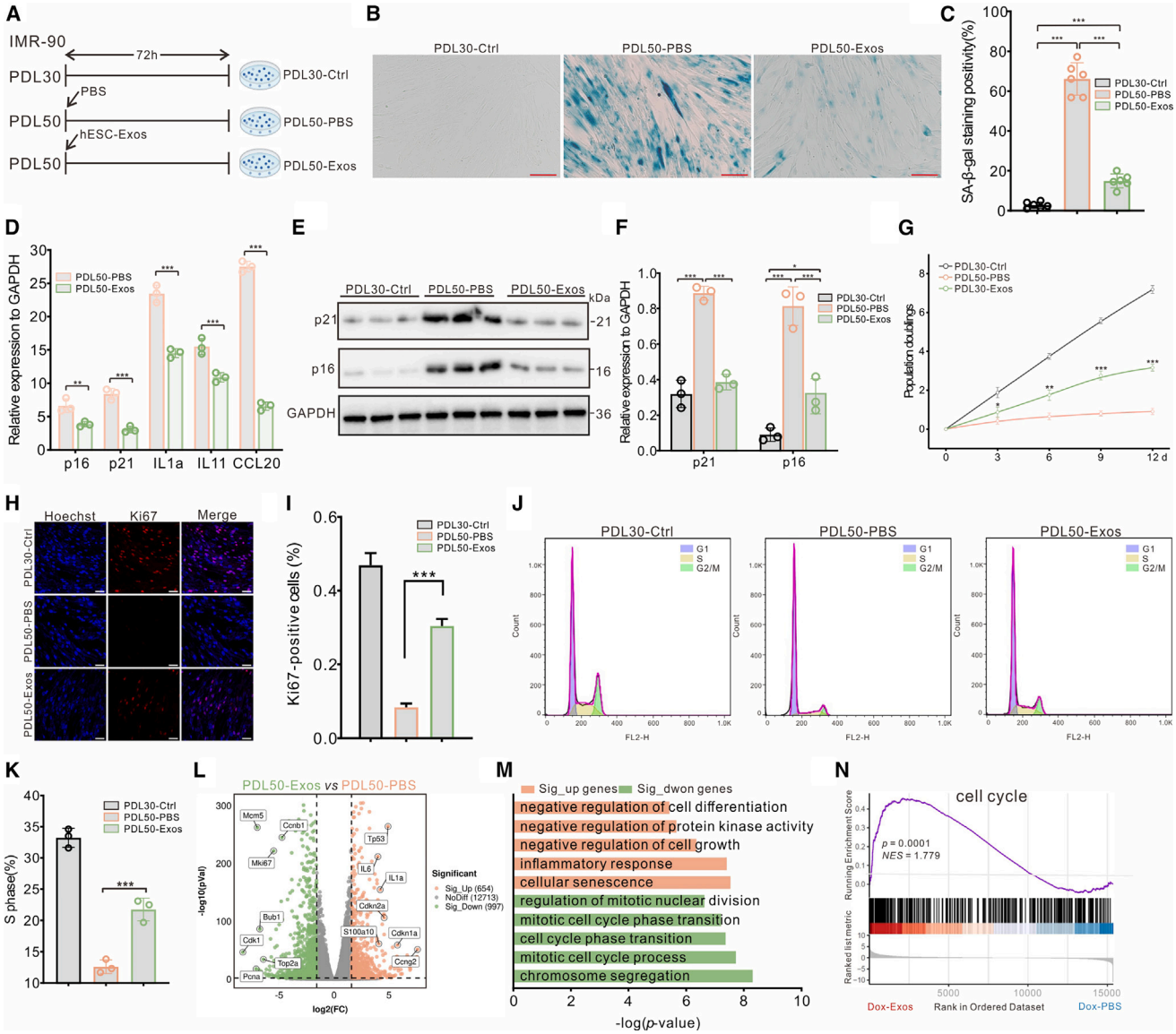

Figure 1. hESC-Exos rejuvenates senescent IMR-90 cells

(A) Schematic diagram of hESC-Exos treating senescent PDL50 IMR-90 cells. PDL30 IMR-90 cells were set as young control.

(B) SA-β-gal staining of PDL30-Ctrl, PDL50-PBS, and PDL50-Exos IMR-90 cells.

Scale bar: 50 μm.

(C) Proportion of SA-β-gal staining-positive cells. Six independent biological replicates were used for each experiment.

(D) RT-qPCR analysis of senescence-related genes. The experiment was independently repeated three times. Gene expression in PDL50-PBS and PDL50-Exos IMR-90 cells was normalized to that in PDL30-Ctrl IMR-90 cells.

(E) Western blot analysis of p21 and p16 in PDL30-Ctrl, PDL50-PBS, and PDL50-Exos IMR-90 cells. GAPDH was used as a loading control.

(F) Quantification of p21 and p16 expression relative to GAPDH expression.

(G) Growth curves of PDL30-Ctrl, PDL50-PBS, and PDL50-Exos IMR-90 cells.

(H) Immunofluorescence images of Ki67 in the PDL30-Ctrl, PDL50-PBS, and PDL50-Exos IMR-90 cells. Scale bar: 100 μm.

(I) Quantification of Ki67-positive cells. Three independent replicates were used for each experiment.

(J) FCM cell cycle analysis for PDL30-Ctrl, PDL50-PBS, and PDL50-Exos IMR-90 cells.

(K) Statistical analysis of the percentage of S-phase cells in (J). Three independent replicates were used for each experiment.

(L) Volcano plot showing gene expression differences between PDL50-PBS and PDL50-Exos IMR-90 cells ($p < 0.01$, $|\log_2 FC| \geq 2$).

(M) GO analysis of differently expressed genes from (H).

(N) GSEA score of the cell cycle module in PDL50-PBS and PDL50-Exos IMR-90 cells.

Data are shown as mean ± SEM. Significance was determined by one-way ANOVA followed by Tukey's post hoc test (C, D, F, I, and K) and two-way ANOVA (G). *$p < 0.05$, **$p < 0.01$, and ***$p < 0.001$.

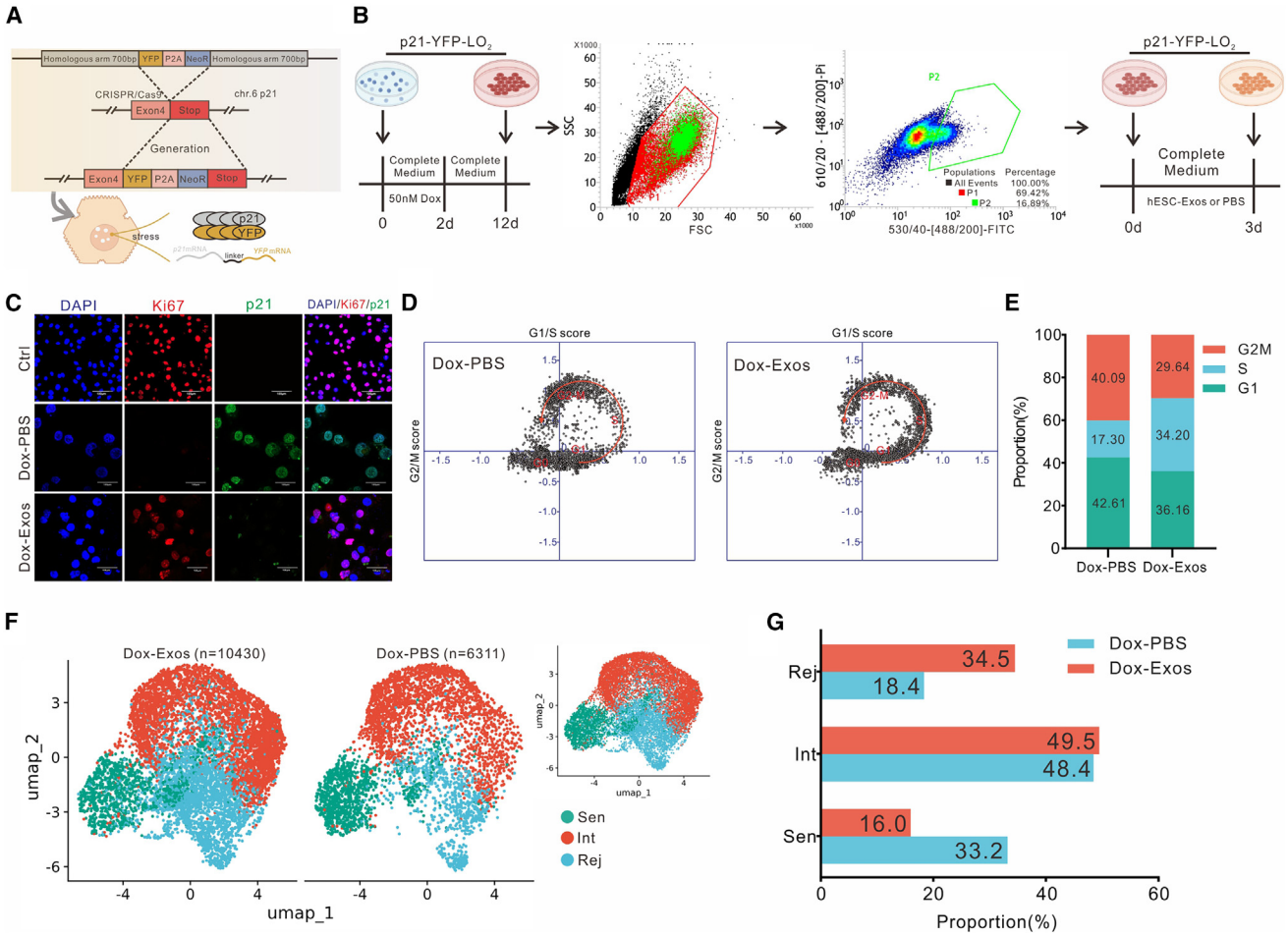

Figure 2. hESC-Exos reverse proliferative arrest of SnCs at single-cell resolution

(A) Schematic illustration of generating p21-YFP senescence reporter cell line.

(B) Sorting of YFP-positive SnCs by FCM.

(C) Immunofluorescence images of Ki67 and p21 in Ctrl, Dox-Exos, and Dox-PBS p21-YFP LO2 cells. Scale bar: 100 μm.

(D) Cell cycle trajectory inferred from scRNA-seq.

(E) Stacked bar plots showing the proportion of cells in different cell cycle phases.

(F) UMAP visualization of enrolled cells.

(G) Bar plots showing the proportion of cell subsets.

Ctrl, p21-YFP LO2 cells without Dox treatment. Dox-Exos, Dox-treated p21-YFP LO2 cells exposed to hESC-Exos. Dox-treated p21-YFP LO2 cells were then incubated with PBS. Sen, senescent cells; Int, cells in an intermediate state; Rej, rejuvenating cells.

hESC-Exos ameliorated aging-related phenotypes, such as sparse and gray hair, at the 30th month (Figure S2D). Notably, aging-Exos mice did not manifest aging-related features of bladder overactivity based on the significantly reduced urine spot number (Figure S2E). The body weight of aging-Exo mice was higher than that of aging-PBS mice from 25 to 30 months of age (Figure 3C).

Aging compromises physiological attributes, including a decline in physical fitness, cognitive function, and learning abilities.[1] In the test of uniformly accelerated rotational motion, aging-Exos mice showed favorable performance characterized by a notable extension of the descent duration compared with aging-PBS mice (Figure 3D). Similar results were observed in the uniform-speed rotarod test at 30 months (Figure 3E). Grip strength was also improved in the comparison between aging-Exos and aging-PBS mice (Figure 3F). In the water maze test, aging-Exos mice spent shorter time locating the platform than aging-PBS mice (Figures 3G and 3H). Moreover, hESC-Exos treatment increased the time spent by aging-Exos mice in the target quadrant during the memory phase compared with aging-PBS (Figures 3I and 3J).

To address the effect of hESC-Exos on age-related chronic inflammation,[28] we performed a cytokine array assay using mouse serum. The levels of pro-inflammatory cytokines were significantly reduced following treatment of hESC-Exos with aging-Exos (Figure S2F; Table S3). Quantification of interleukin (IL)-1β, interferon (IFN)-γ, IL-6, and tumor necrosis factor alpha (TNF-α) via enzyme-linked immunosorbent assay (ELISA) further confirmed a marked decrease in the aging-Exos group (Figure 3K). Moreover, SA-β-gal staining demonstrated an accumulation of SnCs in aged tissues,

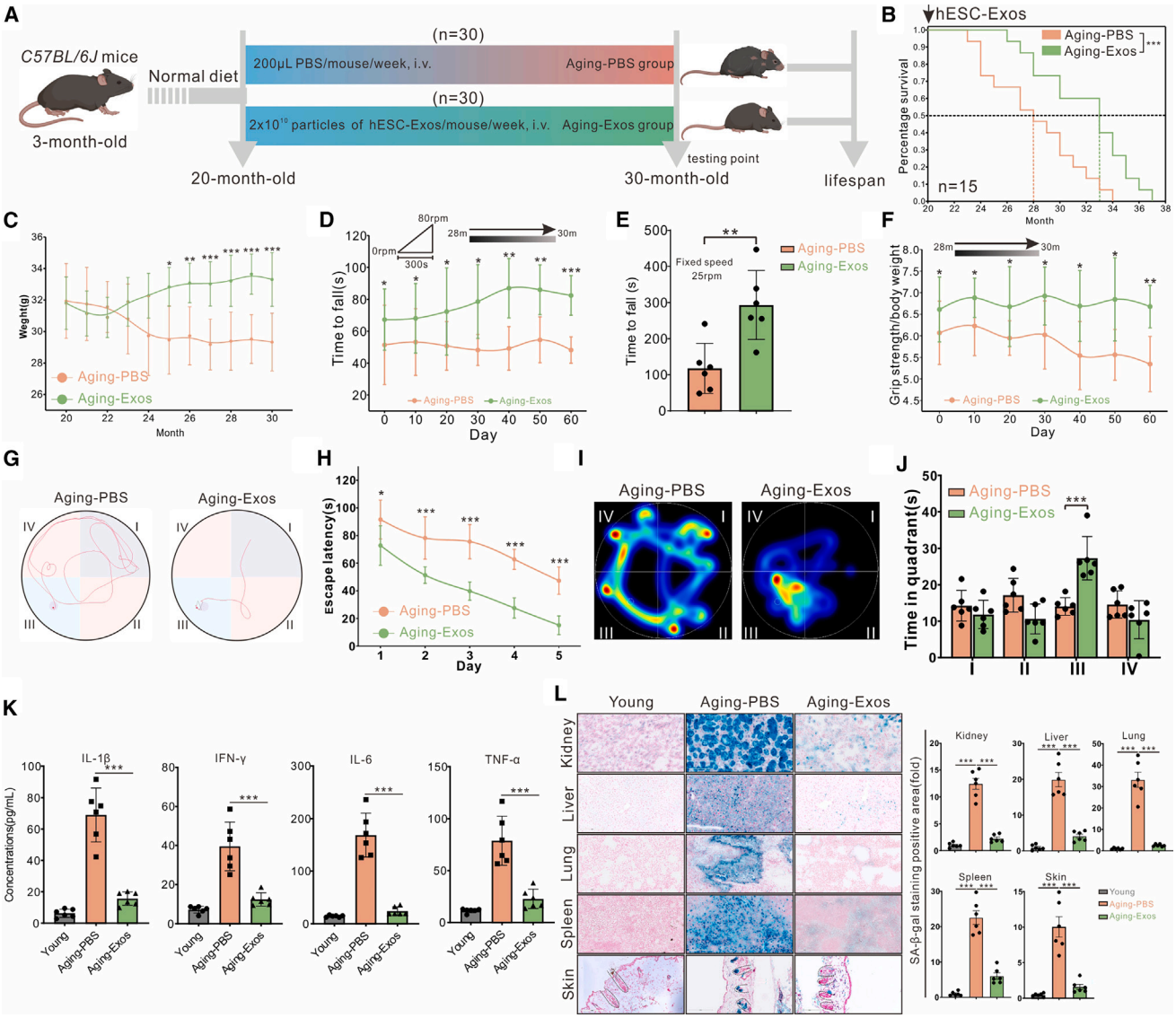

Figure 3. hESC-Exos treatment rejuvenates aging mice

(A) Schematic diagram of mice subjected to hESC-Exos or PBS administration starting at 20 months (feeding plan A in STAR Methods). The 30th month was set as a testing point.

(B) Survival curves of the aging-PBS and aging-Exos groups (n = 15 per group).

(C) Dynamic weight monitoring of mice from 20 to 30 months.

(D) The rotarod test was performed once every 10 days from months 28 to 30 under the condition of increasing the rotational speed from 8 to 80 rpm within 300 s; n = 6.

(E) Comparison of the falling time between the aging-PBS and aging-Exos groups at a fixed speed of 25 rpm at the 30th month; n = 6 per group.

(F) The grip-strength test was performed once every 10 days from months 28 to 30. Limb strength was normalized using the body weight of mice.

(G) Swim paths of mice in the presence of the platform (learning phase).

(H) Escape latencies in the learning phase; n = 6 per group.

(I) Swim paths of mice in the absence of the platform (memory phase).

(J) Time spent by mice in each quadrant; n = 6 per group.

(K) ELISA assay detected the levels of inflammatory factors in the serum. n = 6 per group.

(L) SA-β-gal staining analysis of kidney, liver, lung, spleen, and skin tissues (n = 6 per group). Left, representative micrograph of SA-β-gal. Right, quantification of SA-β-gal staining-positive signaling. Scale bar: 200 μm.

Data are shown as mean ± SEM. Significance was determined by one-way ANOVA followed by Tukey's post hoc test (J–L), two-way ANOVA test (C, D, F, and H), Student's t test (E), or log rank (Mantel-Cox) test (B). *p < 0.05, **p < 0.01, and ***p < 0.001.

which was reversed by hESC-Exos administration (Figure 3L). Additionally, hESC-Exos treatment reduced the expression of the DNA damage marker γ-H2AX and increased the expression of H3K9me3, a marker associated with genomic stability (Figure S2G).[12] Pathological analysis further revealed hESC-Exos improved the pathological characteristics of aging tissues, including skin wrinkling, inflammatory responses, and other degenerative changes (Figure S2H). Collectively, hESC-Exos treatment reversed the aging phenotype of mice to a more rejuvenated state.

hESC-Exos treatment remodeled the proliferation process in aging mice

Next, we investigated the effects of hESC-Exo treatment on cell proliferation *in vivo*. We performed scRNA-seq on the liver and skin tissues isolated from aging-Exos and aging-PBS mice (n = 3 per group). The single-cell transcriptomic data were then integrated with previously reported sequencing data from liver and skin tissues isolated from 3-month-old C57BL/6J male mice (set as the young group).[29] We identified 28 cell clusters within the liver and 25 cell clusters within the skin using the DoubleFinder and Seurat R packages.[25] Cell types were identified based on canonical cell type-specific markers (Figures S3A–S3D; Table S2).[30] Notably, hESC-Exos treatment remodeled the composition of cell types in aging mice (Figures S4A and S4B; Table S2) and reversed the age-related gene expression changes (Figures S4C–S4F; Table S2).

We then extracted the scRNA transcriptome of mitotic cells based on Mki67 expression and identified the cell cycle phases of these cells in the liver and skin tissues using the built-in cell cycle scoring algorithm in Seurat R.[31] Aging diminished the proportion of S-phase cells in both liver and skin tissues, which was reversed by hESC-Exos treatment (Figure 4A; Table S2). The DEGs were then overlapped with genes regulating the cell cycle pathway retrieved from the PathCards database (https://pathcards.genecards.org/),[32] and the shared subset was termed hub cell cycle-related genes (CCGs). The CCGs between aging-PBS and young mice and between aging-PBS and aging-Exos mice were identified and referred to as "aging CCGs" and "Exos CCGs," respectively. The shared genes between aging CCGs and Exo CCGs were identified as rescue CCGs (Figure 4B; Table S2). Notably, 10 rescue CCGs prominently emerged after overlapping rescue CCGs in the liver and skin tissues, including four downregulated rescue CCGs (*Cdkn2a*, *Cdkn1a*, *Cdkn1b*, and *Ccng2*) and six upregulated rescue CCGs (*E2f1*, *Mki67*, *Top2a*, *Cdk1*, *Ccnb1*, and *Pcna*) (Figure 4C).

Next, we extracted the scRNA transcriptome of mitotic cells based on *Mki67* expression.[33] After UMAP dimensionality reduction and clustering, the cell clusters were categorized as Rej cells, characterized by high expression of *Mki67* and low expression of *Cdkn1a*, and Sen cells, marked by high expression of *Cdkn1a* and low expression of *Mki67*. Intermediate cells exhibited intermediate expression levels of both *Cdkn1a* and *Mki67* (Figures S3E and S3F). Pseudotemporal trajectory analysis revealed the pivotal factors that drive the transition from the Sen-to-Rej cell state (Figures 4D, 4E, and S3G–S3I; Table S2). In liver tissues, module 1 encompassed genes upregulated during Sen-to-Rej conversion, such as *Selenop*, *Pcna*, *Mki67*, and *Top2a*, whereas module 2 contained downregulated genes during Sen-to-Rej differentiation, including *Cdkn1a*, *Ccl2*, *Ptprb*, and *Ccng2* (Figure 4D). In skin tissues, module 1 comprised genes upregulated during Sen-to-Rej differentiation, including *Krt15*, *Mki67*, *Atf3*, and *Fabp5*. By contrast, module 2 genes represented those downregulated during Sen-to-Rej differentiation, including *S100a8*, *S100a9*, *Ccng2*, and *Cdkn1a* (Figure 4E).

Here, we focused on the shared genes, *Cdnk1a* and *Ccng2* (also termed rescue CCGs), identified in pseudotemporal trajectory inferences, which contribute to cellular senescence in both liver and skin tissues. Immunofluorescence staining further confirmed that hESC-Exos treatment repressed the expression of *Cdkn1a* and *Ccng2* in both aging liver and skin (Figure 4F). Collectively, Cdkn1a and Ccng2 serve as essential factors that promote cell cycle arrest and contribute to aging. hESC-Exos treatment reversed cell cycle arrest in SnCs, thus promoting rejuvenation by suppressing the expression of *Cdkn1a* and *Ccng2*. These data indicate that hESC-Exos treatment partially restored the proliferation-related signature of aging mice.

Enriched miR-302b in hESC-Exos repressed cell cycle checkpoints *Cdkn1a* and *Ccng2*

The hESC-Exos encapsulate a diverse array of bioactive substances involved in the aging process.[15] High-throughput sequencing revealed enrichment of miR-302b-3p in hESC-Exos (Figure 5A). To further ascertain the miR-302b content in hESC-Exos, we performed an absolute quantitative PCR (qPCR) assay, establishing a linear relationship between miR-302b copy number and its absolute quantity ($y = -0.8711 + 11.798$, $R^2 = 0.9854$) (Figure S5A). Accordingly, the concentration of miR-302b-3p in hESC-Exos was calibrated to (306 ± 50.6) pmol per 1,000 particles of hESC-Exos, as determined through three independent replicates (Figures S5B and S5C).

The miR-302 family plays an essential role in cellular reprogramming and stemness maintenance; however, data regarding its impact on cell proliferation and aging process are limited.[34,35] Therefore, we performed Ago2 crosslinking immunoprecipitation sequencing (Clip-seq) analysis to identify the regulatory signaling and target genes of miR-302b (Figure 5B; Table S1).[36] To identify high-confidence binding sites, we applied conditional filtering to those with distinctive signal peaks, requiring at least 2-fold change. The obtained candidate sites overlapped with predicted sites from the miRanda and TargetScan databases (Figure 5C).[37,38] Gene Ontology (GO) analysis revealed that the candidate targets of miR-302b were predominantly enriched in regulating of the mitotic cell cycle, cell division, and DNA damage response (Figure 5D). Notably, miR-302b displayed a low minimum free energy (MFE) with both the 3′ UTR of *Cdkn1a* and *Ccng2*, measuring −12.84 and −16.15 kcal/mol, respectively (Figure 5E).

To validate the reliability of our analysis, we performed dual-luciferase assays by co-transfected Renilla luciferase mRNA harboring the 3′ UTR sequence of *Cdkn1a* or *Ccng2*, along with luciferase mRNA and miR-302b mimics, into IMR-90 cells and NCTC1469 cells (a mouse normal liver cell line). Compared with vehicle transfection, the relative fluorescence activities of *Cdkn1a* and *Ccng2* were markedly diminished (Figures 5F and S5D). This confirms that miR-302b targets the 3′ UTR sequence of *Cdkn1a* and *Ccng2*, thereby regulating their transcription.

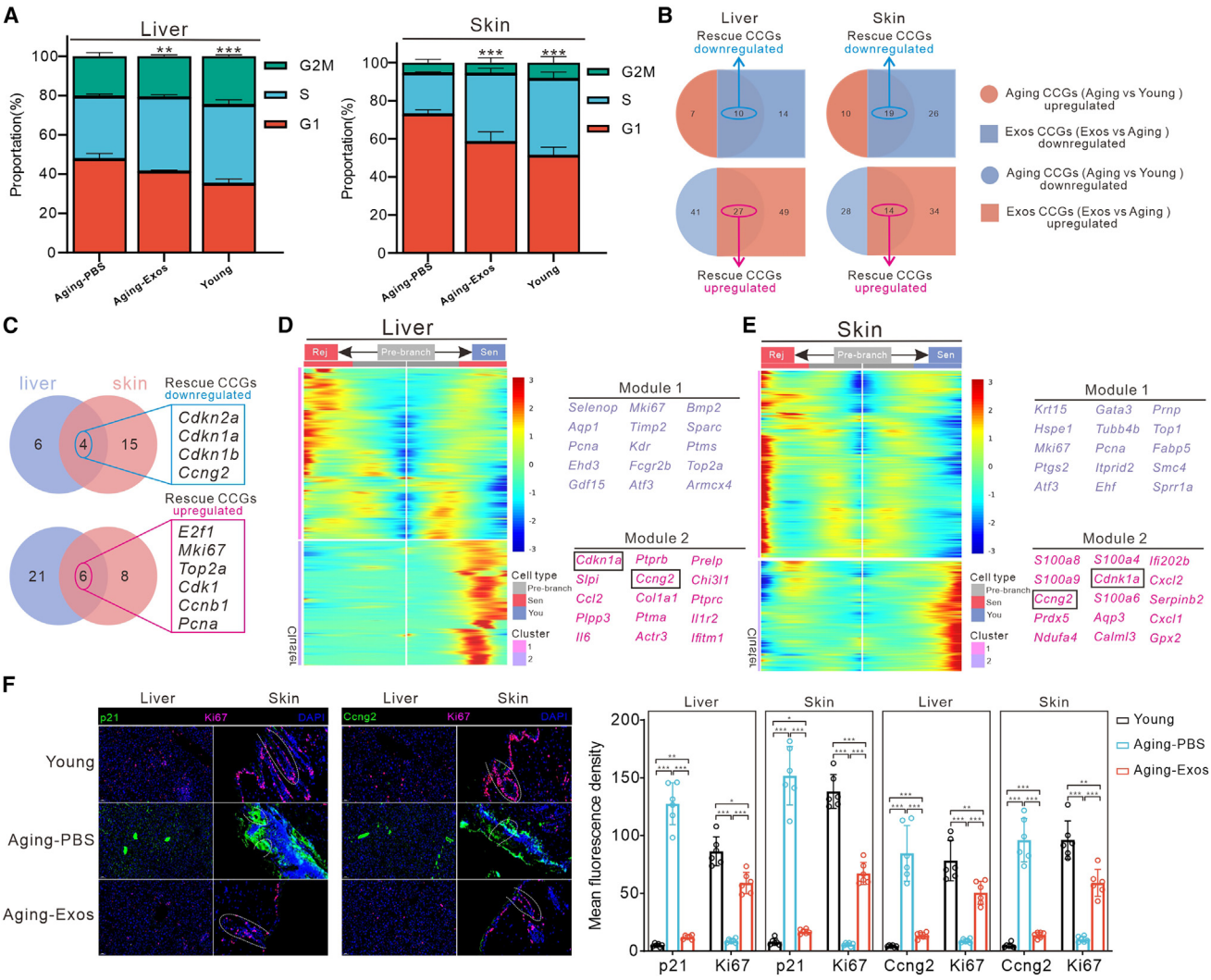

Figure 4. hESC-Exos treatment remodels the proliferation process in aging mice

(A) Stacked bar plots showing the proportion of cell subsets in the liver and skin in different cell cycle phases.

(B) Venn diagrams showing the numbers of aging, Exos, and rescue cell cycle-related genes with significant differential expression (CCGs). The overlapping regions indicate the number of downregulated rescue CCGs (top row) and upregulated rescue CCGs (bottom row).

(C) Venn diagrams depict the shared downregulated rescue CCGs (top) and upregulated rescue CCGs (bottom) between liver and skin tissues.

(D and E) Differential gene heatmaps of the liver (E) and skin (F) across Int-to-Sen (right arrow) and Int-to-Rej (left arrow) pseudotemporal trajectory, grouped by hierarchical clustering (k = 2). Gene co-expression modules and exemplar genes from each module are labeled (right). Sen, senescent cells; Int, cells in an intermediate state; and Rej, rejuvenating cells.

(F) Representative immunofluorescent micrographs of p21 (left green), Ccng2 (right green), Ki67 (cerise), and DAPI (blue) in liver and skin (n = 6 per group). Left, representative fluorescence staining micrograph. Right, the quantification of fluorescence signal.

Data are shown as means ± SEM. Significance was determined by one-way ANOVA followed by Tukey's post hoc test (A and F). *p < 0.05, **p < 0.01, and ***p < 0.001.

Additionally, liver and skin tissues from aging-Exos mice exhibited increased miR-302b levels compared with those from aging-PBS mice, with values of 582.05 ± 42.38 vs. 0.71 ± 0.12 pmol/g in livers and 32.16 ± 6.09 vs. 0.05 ± 0.01 pmol/g in skins, respectively (Figure S5E; Table S4). These results also corresponded to a decrease in *Cdkn1a* and *Ccng2* levels in the liver and skin tissues of aging-Exos mice compared with those in aging-PBS mice.

To validate the rejuvenation effect of miR-302b on SnCs, we transfected miR-302b mimics or negative controls into PDL50 IMR-90 cells. Absolute qPCR was used to measure miR-302b levels, demonstrating a significant increase after miR-302b mimic transfection (Figure 5G; Table S4). The enhanced SA-β-gal activity in PDL50 IMR-90 cells was significantly counteracted by miR-302b overexpression (Figures 5H and 5I). Flow cytometry analysis further showed that miR-302b overexpression ameliorated the reduction in the proportion of S-phase cells (Figures 5J and 5K). The increased expression levels of p21 and Ccng2 in senescent PDL50 IMR-90 cells were also attenuated by miR-302b treatment (Figures 5L and 5M). In summary,

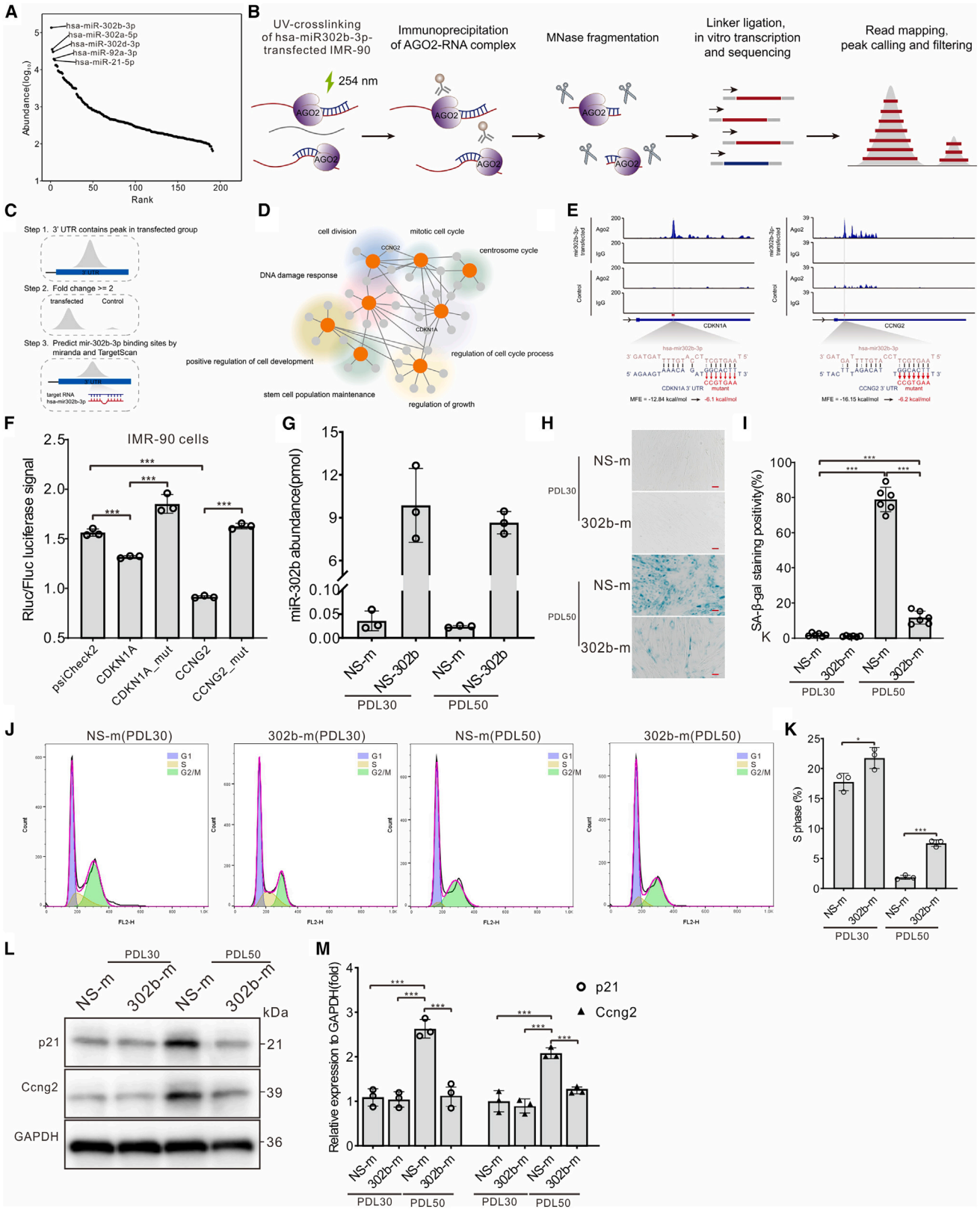

(legend on next page)

we deduced that miR-302b facilitated rejuvenation by repressing the expression of *Cdkn1a* and *Ccng2 in vitro*.

miR-302b treatment rejuvenated aging mice

Next, we investigated whether miR-302b treatment induce rejuvenation *in vivo*. Exosomes derived from 293F cells were electro-transfected with miR-302b mimics, producing exosomes designated as Exos-302b (Figure 6A). Quantification via qPCR revealed a concentration of miR-302b in Exos-302b at 62.39 ± 81.29 pmol per 10^{10} particles (Figure S5F; Table S4). Mice aged 25 months, exhibiting sparse dorsal fur akin to approximately 70 years of age in humans, were randomly divided into the aging-302b group and aging-NC group based on body weight. The experimental endpoint, designated as 5 months after administration (30th month), was chosen (Figure 6B). Throughout consecutive administrations of Exos-302b, we monitored changes in dorsal fur. Restored hair growth, which was originally shed due to natural aging, was restored after miR-302b delivery (Figure 6C). Aging-302b mice exhibited increased body weights compared with aging-NC mice from 28 to 30 months of age (Figure 6D).

During the monthly physical tests, aging-302b mice exhibited better performance from months 27 to 30 compared with aging-NC mice (Figure 6E). Grip strength in aging-302b mice also significantly improved starting at month 28 (Figure 6F). In the water maze test, aging-NC mice showed a slight shortening in the time taken to locate the platform from months 25 to 30. Conversely, aging-302b mice exhibited a clear decline in escape latency, with considerably shorter starting times starting at month 28, compared with aging-NC mice (Figure 6G). Additionally, we recorded the time spent by the mice in the target quadrant during the memory phase within 1 min from months 25 to 30. While the time spent by aging-302b mice in the target quadrant slightly increased, aging-PBS mice showed a significant increase. Moreover, aging-302b mice demonstrated superior memory performance compared with aging-NC mice, indicated by notably extended residence time in the target quadrant (Figure 6H).

In addition, ELISA and cytokine array assays revealed that miR-302b delivery alleviated chronic inflammation in the circulation of aging mice (Figures 6I and S5G; Table S3). We evaluated the effects of miR-302b delivery to aging tissues, including the kidneys, liver, lungs, spleen, and skin. SA-β-gal staining revealed that miR-302b delivery reversed the SnC accumulation in the above-aged tissues (Figure 6J). Additionally, miR-302b delivery reduced the expression of the DNA damage marker γ-H2AX and increased the expression of H3K9me3, a marker associated with genomic stability (Figures S5H and S5I). Absolute qPCR was used to determine the miR-302b load in tissues. The livers, skins, and brains of aging-302b mice contained significantly elevated miR-302b load compared with aging-NC mice (620.22 ± 131.07 vs. 0.89 ± 0.07 pmol/g in livers; 31.27 ± 7.36 vs. 0.06 ± 0.03 pmol/g in skins; 49.33 ± 13.06 vs. 0.02 ± 0.004 pmol/g in brains (Figure S5J; Table S4). Immunofluorescence staining confirmed that miR-302b delivery repressed Cdkn1a and Ccng2 expression in the aging liver, skin, and brain (Figure 6K). Overall, miR-302b inhibited the expression of Cdkn1a and Ccng2 in SnCs, restoring their proliferative ability and promoting rejuvenation.

Long-term miR-302b delivery decelerated the aging process and raised no safety concerns

We next investigated the long-term safety concerns associated with miR-302b delivery (Figure 7A). Weight monitoring revealed that aging-302b mice maintained significantly higher body weight compared with aging-NC mice from 27 months onward, indicating miR-302b delivery may mitigate progressive weight loss associated with aging (Figure 7B). Moreover, the median lifespan of aging-302b mice was extended by 137 days compared with aging-NC mice (∼15.4% increase), with a mortality hazard ratio (HR) reduced to 38% (Figure 7C). Mixed-effects Cox regression revealed a significantly lower risk of death in aging-302b mice compared with aging-NC mice. Although the HR of death between male and female mice was not significant ($p > 0.05$), the median lifespan extension seemed to be more evident in male than female aging-302b mice (182 vs. 143 days, 22.1% vs. 14.9%) (Figure 7C). In addition, we compared the maximum lifespan (85th percentile) between aging-NC and aging-302b mice using Mann-Whitney U test and Fisher's exact test. Both tests demonstrated that the maximum lifespan was significantly increased by 12.13% in aging-302b mice with both sexes combined. For each sex, the maximum lifespan extension was statistically significant in both male (9.86%) and female (13.99%) aging-302b mice (Figure 7D).

Figure 5. Enriched miR-302b in hESC-Exos represses cell cycle checkpoints *Cdkn1a* and *Ccng2*

(A) miRNAs in hESC-Exos. The top five are listed.
(B) Schematic illustration of the workflow for identifying miR-302b targets using Ago2 Clip-seq in miR-302b-transfected IMR-90 cells.
(C) Identification of the binding sites between miR-302b and the 3′ UTR of target mRNAs using bioinformatics strategy.
(D) GO enrichment network of the candidate targets of miR-302b. Gray nodes and edges denote the candidate target of miR-302b. The individual pathways are shown in orange nodes.
(E) The base pairing between miR-302b and the 3′ UTR of *Cdkn1a* (left) or *Ccng2* (right). Red arrows indicate the mutation sites in the 3′ UTR of *Cdkn1a* or *Ccng2*. MFE, minimum free energy (dark, MFE between miR-302b and WT 3′ UTR fragment; red: MFE between miR-302b and mutant 3′ UTR fragment).
(F) Luciferase activity was measured in IMR-90 cells co-transfected with miR-302b mimics and luciferase reporter plasmids containing wild type or mutant.
(G) qPCR detection of miR-302b load in IMR-90 cells.
(H) SA-β-gal staining of IMR-90 cells with different treatments.
(I) Quantification of the percentage of SA-β-gal staining-positive cells. Six independent replicates were performed.
(J) FCM depicting the cell cycle distribution of IMR-90 cells with different treatments.
(K) Statistical analysis of S-phase percentage in (J).
(L) Western blot analysis of p21 and Ccng2 expression in IMR-90 cells with different treatments. GAPDH was set as an internal reference.
(M) Quantification of p21 and Ccng2 expression in (L) relative to GAPDH.
(G–M) IMR-90 cells were transfected with miRNA-negative control (NS-m) or miR-302b mimics (302b-m) for 48 h.
Data are shown as means ± SEM. Significance was determined by one-way ANOVA followed by Tukey's post hoc test (F, I, K, and M). $^{*}p < 0.05$, and $^{***}p < 0.001$.

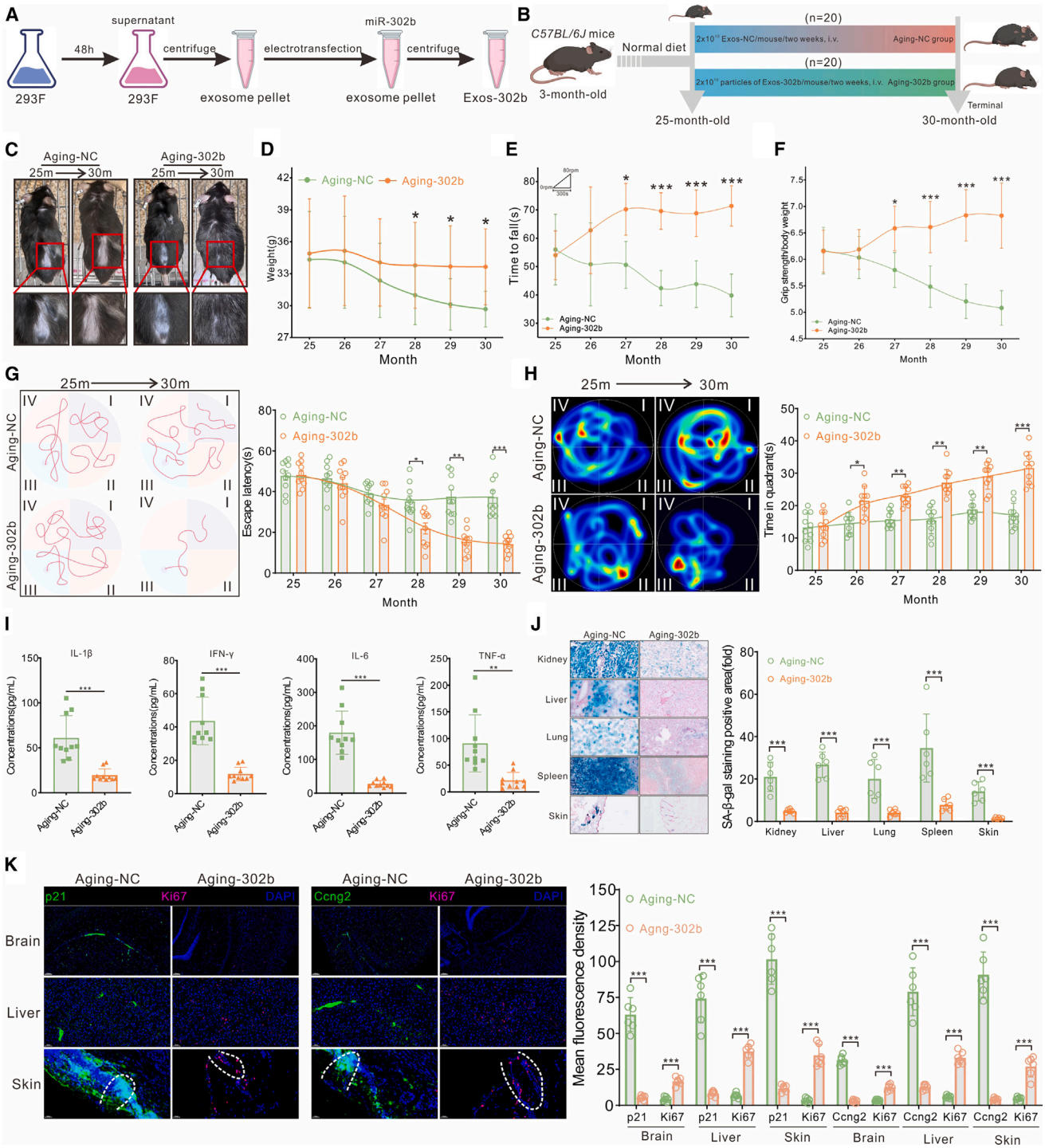

Figure 6. miR-302b treatment rejuvenates aging mice

(A) 293F-derived exosomes were transfected with miR-302b mimics via electroporation, named Exos-302b. 293F-derived exosomes electroporated with miRNA-negative control, named Exos-NC.

(B) Schematic diagram of mice subjected to Exos-302b or Exos-NC administration starting at 25 months (feeding plan B in STAR Methods). The 30th month was set as the testing point.

(C) Morphological changes of mice from months 25 to 30 after administration with Exos-302b or Exos-NC.

(D) Weight dynamic monitoring of mice from months 25 to 30; $n = 10$ per group.

(E) The rotarod test was performed every month from months 25 to 30 under the condition of increasing the rotational speed from 8 to 80 rpm within 300 s; $n = 10$ per group.

(legend continued on next page)

The delivery of miR-302b improved external appearance of aging mice, including increased dorsal hair coverage and reduced spinal curvature (Figure S6A). In spite of longer lifespan, aging-302b mice showed no significant differences in tumor and disease burdens compared with aging-NC mice, according to postmortem pathological examinations, and the causes of death were similar between the two groups (Figures 7E and 7F). Pathological analysis of mice aged 30–35 months revealed that miR-302b delivery alleviated many age-associated histological changes across multiple organs, including increased epidermal thickness, decreased skin keratinization, and the rescue of spleen involution and lymphoid depletion in the white pulp (Figures S6B and S6C).[12] Additionally, miR-302b delivery restored the proliferation rates to levels approaching those of 12-month-old mice, as indicated by Ki67 staining in multiple organs (Figures S6D and S6E). To address the molecular impact of miR-302b delivery, we performed bulk RNA-seq on various tissues from young, aging-NC, and aging-302b mice (Table S5), revealing that miR-302b restored proliferation hallmarks and reduced inflammation hallmarks across all four aged tissues (Figure 7G).

Collectively, long-term administration of miR-302b extended the lifespan of aging mice, ameliorated visible signs of aging, did not increase tumor or disease burden, reversed the decline in cellular proliferative capacity within aging tissues, alleviated aging-related transcriptomic signatures, and thereby effectively decelerated the aging process.

DISCUSSION

miR-302b enriched in hESC-Exos rejuvenated SnCs by reversing proliferative arrest

Cell proliferation is essential for maintaining tissue functionality.[9,39] However, Hayflick's limit gradually disables cell proliferation, resulting in senescence and programmed cell death.[20] *Cdkn1a* and *Ccng2* accumulate continuously during this process, directly repressing the activation of the Cdk/cyclin complex, which initiates cell cycle arrest.[40,41] Exosomal miR-302b reverses cell cycle arrest in SnCs by directly targeting *Cdkn1a* and *Ccng2*, thereby facilitating proliferation and achieving global rejuvenation. Our findings show that miR-302b alleviates age-related inflammation, improves physical and cognitive function, and extends lifespan in aged mice without increasing disease burden. These results suggested that miR-302b delivery is a potential therapeutic strategy for ameliorating aging and counteracting age-related diseases.

SnCs are characterized by permanent cell cycle arrest and respond to various intrinsic and extrinsic stressors.[13,21] Central to this process are the p53/p21 and p16INK4a/Rb pathways, which enforce cell cycle arrest, thereby preventing damaged or aged cells from proliferating.[8,42] miR-302b treatment effectively reverses the proliferative capacity of SnCs, challenging the dogma of irreversible growth arrest.[20] This is particularly significant in both replicative and drug-induced senescence models. Furthermore, the rejuvenation of miR-302b suggests that one of its key mechanisms may be the reactivating of the cell cycle in SnCs. This led to an increase in cell proliferation, helping to replenish and rejuvenate the aging tissue.

Several studies have suggested that miR-302b plays a role in cellular reprogramming, potentially reverting mature cells to a more pluripotent state.[43] Cellular reprogramming involves a significant shift in cell identity, erasing differentiated states and acquiring stem cell-like properties.[44] However, our findings demonstrate that miR-302b treatment of SnCs and aging mice leads to a reversal of senescence markers and an improvement in cellular and organismal functions. This improvement is primarily attributed to the restoration of cell proliferation rather than a change in cell identity. miR-302b exerts its rejuvenating effects by targeting specific pathways involved in senescence, such as the downregulation of cell cycle inhibitors *Cdkn1a* and *Ccng2*, known contributors to the maintenance of the senescent state.[40,45,46] By mitigating these inhibitions, miR-302b enables the resumption of cell division in SnCs, promoting tissue regeneration and overall rejuvenation in aging mice.

Various strategies targeting SnCs have shown promise in aging rodents,[6,10,47] yet face challenges in effectively compensating for functional cells post-SnCs clearance and disrupting immune surveillance.[9,48,49] To address these limitations, we propose the Senoreverse strategy to achieve rejuvenation by reversing the proliferation capacity of SnCs. Our study revealed that hESC-Exos could achieve systemic rejuvenation without tumorigenic effects *in vivo*. Moreover, the enrichment of miR-302b in hESC-Exos likely contributes to their rejuvenating effects. miR-302b offers a viable path for reversing the proliferative capacity of SnCs and ameliorating age-related diseases, implying the potential of miR-302b as a nucleic acid therapeutic candidate for Senoreverse.

Limitations of the study

Administration of miR-302b for approximately 24 months did not increase tumor burden in mice. However, its potential tumorigenicity in broader biological contexts, such as tumor-prone mouse models, remains uncertain. This study primarily focused on the effects of miR-302b on proliferative cells, leaving its role in non-proliferative cells unexamined. The pharmacokinetic properties of miR-302b, including its distribution, metabolism, and excretion across different tissues, are still poorly understood. Future studies

(F) The grip-strength test was performed monthly from months 25 to 30. Limb strength was normalized using the body weight of mice; $n = 10$ per group.
(G) Swim paths of mice in the presence of the platform (learning phase) (left) and the escape latencies in the learning phase from months 25 to 30 (right); $n = 10$ per group.
(H) Swim paths of mice in the absence of the platform (memory phase) (left) and the time spent in each quadrant from months 25 to 30; $n = 10$ per group.
(I) ELISA detected the levels of inflammatory factors in the serums from aging-NC and aging-302b groups. $n = 10$ per group.
(J) SA-β-gal staining analysis of kidney, liver, lung, spleen, and skin tissues ($n = 10$ per group). Scale bar: 200 μm.
(K) Left, representative immunofluorescent micrographs of Cdkn1a (left green), Ccng2 (right green), Mki67 (cerise), and DAP (blue) in brain, liver, and skin ($n = 6$ per group). Scale bar: 50 μm. Right, quantification of fluorescence signal.
Data are shown as means ± SEM. Significance was determined by two-way ANOVA (D–H), one-way ANOVA with Tukey's post hoc test (J and K), or Student's t test (I). $^{*}p < 0.05$, $^{**}p < 0.01$, and $^{***}p < 0.001$.

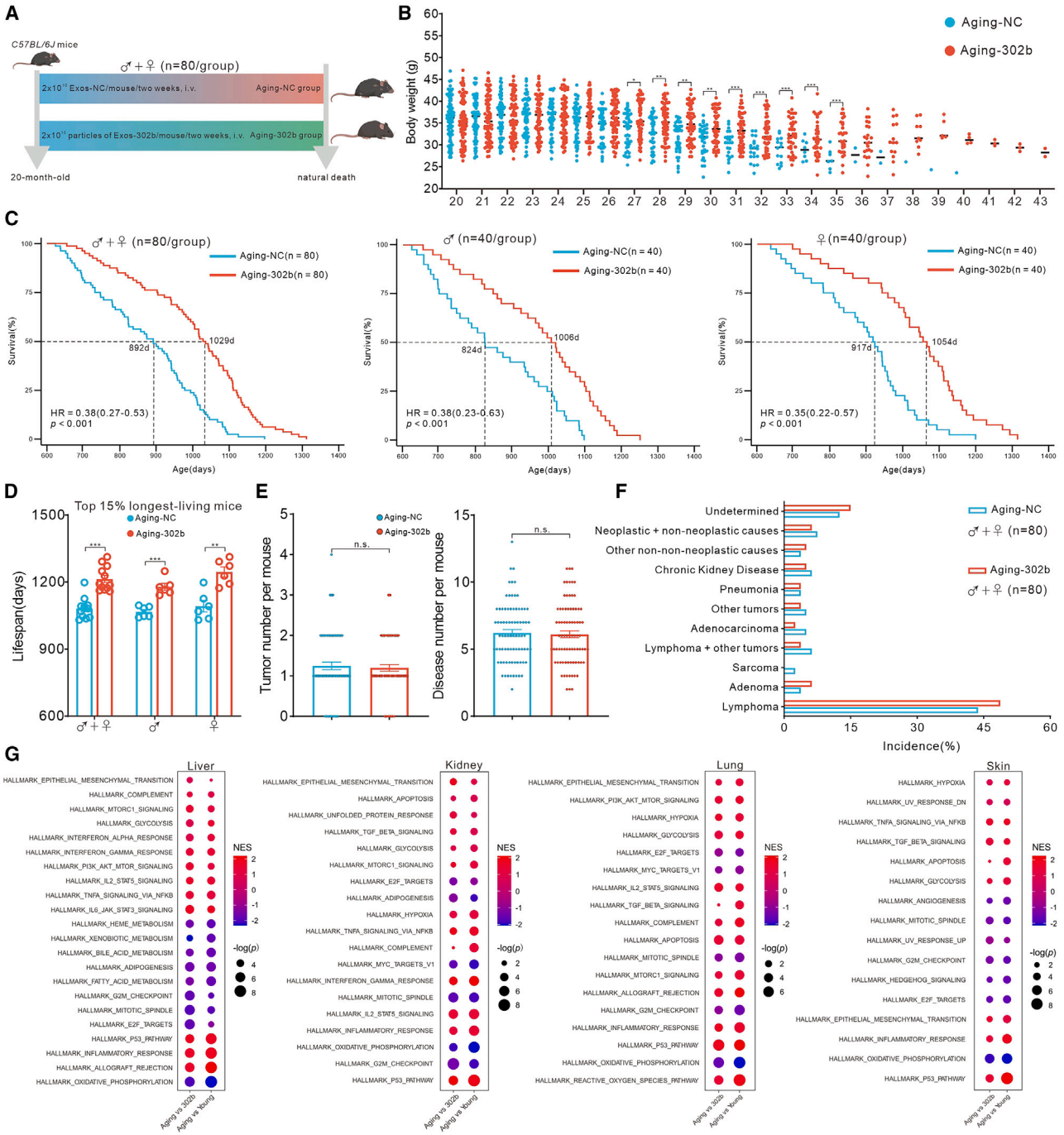

Figure 7. Long-term miR-302b delivery decelerated aging process and raised no safety concerns

(A) Schematic diagram of mice subjected to Exos-302b or Exos-NC administration starting at 20 months. The mice were treated with miR-302b or NC starting from 20 months of age until natural death and received Exos-302b or Exos-NC treatment every 2 weeks (feeding plan C in STAR Methods).

(B) Body weight of aging-NC (n = 80; 40 males, 40 females) and aging-302b (n = 80; 40 males, 40 females) from 20 months to natural death.

(C) Survival curves of aging-NC (n = 80; 40 males, 40 females) and aging-302b (n = 80; 40 males, 40 females) starting at 20 months of age. Male-only and female-only survival curves are shown as well. Median lifespan (days) is indicated.

(D) Lifespan of the top 15% longest-living aging-NC and aging-302b mice (n = 12 for ♂ + ♀ per group; n = 6 for ♂ or ♀ per group).

(E) Tumor burden and disease burden of aging-NC (n = 80; 40 males, 40 females) and aging-302b (n = 80; 40 males, 40 females) at death.

(legend continued on next page)

should address these gaps to comprehensively assess the safety and efficacy of miR-302b as a Senoreverse candidate, thus establishing a solid foundation for its clinical application.

RESOURCE AVAILABILITY

Lead contact

Further information and requests for resources and reagents should be directed to and will be fulfilled by the lead contact, Guangju Ji (gj28@ibp.ac.cn).

Materials availability

All unique/stable reagents generated in this study are available from the lead contact without restriction.

Data and code availability

- All original blot images and quantitative data for the graphs presented in this manuscript are available in Data S1.
- Raw and processed sequencing data were deposited in the GEO: GSE247076.
- All scRNA-seq analysis results, bulk RNA-seq data, and Ago2 Clip-seq data generated in this study have been deposited in Mendeley Data: https://doi.org/10.17632/899tntr9x2.1.
- All analyses were performed using freely available software packages. The custom code used to analyze the RNA-seq data and datasets generated and/or processed in this study is available from the lead contact upon request.

ACKNOWLEDGMENTS

We thank J. Hu for critical reading of this manuscript. This work was supported by grants from High-level Talent Research Start-up Project Funding of Henan Academy of Sciences (232016003 to G.J.), Joint Fund of Henan Province Science and Technology R&D Program (225200810069 to G.J.), Postdocoral Fellowship Program of CPSF (GZB20230809 to Y.B.), National Key Research and Development Project (2019YFA0110400 to G.J.), and National Natural Science Foundation of China (31971051 and 31771562 to G.J.; 32025008 and 32130064 to Y. X.).

AUTHOR CONTRIBUTIONS

G.J., Y.X., Y.B., and H. Wu initiated and planned the study; Y.B. and X.Q. cultured cells, prepared the hEC-Exos, and generated p21-YFP LO2 cells; X.Q. and Y.B. performed the live-cell workstation observation; Y.B., B.L., and Yixuan Liu completed the animal husbandry and management; Y.B. and C.J. performed the single-cell data analysis; Z.C. performed the dual-luciferase assays; Z.C., R.Y., and H.Z. completed the Ago2 Clip-seq analysis; Q.L., L.G., and Yingqi Liu performed the absolute quantitative qPCR detection; X.Q., L.G., Z.Y., and Y.W. performed the animal behavior testing; Y.B., H. Wang, and W.J. performed the histopathological testing; W.J. and C.Z. verified the statistical analysis; Y.Z. and C.Z. advised on the bioinformatics analysis; Y.B., G.J., Y.X., and H. Wu wrote the manuscript.

DECLARATION OF INTERESTS

The authors declare no competing interests.

STAR★METHODS

Detailed methods are provided in the online version of this paper and include the following:

- KEY RESOURCES TABLE
- EXPERIMENTAL MODEL AND STUDY PARTICIPANT DETAILS
  - Mice
  - Treatment plan
- METHOD DETAILS
  - Extraction and identification of hESC-Exos
  - Population doubling assays
  - p21-YFP cell line generation
  - Preparation of doxorubicin-induced SnCs
  - Cell cycle analysis
  - Live-cell workstation observation
  - In vivo safety assessment of hESC-Exos
  - Urine spot assay
  - Immunofluorescence microscopy
  - Postmortem pathological examination
  - Bulk RNA-seq
  - SA-β-gal staining
  - Cytokine array assay of mice serums
  - Absolute quantification of miR-302b by RT-qPCR
  - Preparation of exosomes loaded with miR-302b mimics
  - Luciferase assays
  - Ago2 Clip-seq
  - Mirror water maze
  - Grip strength test
  - Rotarod test
  - Statistical analysis of scRNA-seq data
- QUANTIFICATION AND STATISTICAL ANALYSIS

SUPPLEMENTAL INFORMATION

Supplemental information can be found online at https://doi.org/10.1016/j.cmet.2024.11.013.

Received: December 7, 2023
Revised: September 9, 2024
Accepted: November 25, 2024
Published: January 15, 2025

REFERENCES

1. López-Otín, C., Blasco, M.A., Partridge, L., Serrano, M., and Kroemer, G. (2023). Hallmarks of aging: an expanding universe. Cell *186*, 243–278. https://doi.org/10.1016/j.cell.2022.11.001.
2. Khosla, S., Farr, J.N., Tchkonia, T., and Kirkland, J.L. (2020). The role of cellular senescence in ageing and endocrine disease. Nat. Rev. Endocrinol. *16*, 263–275. https://doi.org/10.1038/s41574-020-0335-y.
3. Campisi, J., and d'Adda di Fagagna, F. (2007). Cellular senescence: when bad things happen to good cells. Nat. Rev. Mol. Cell Biol. *8*, 729–740. https://doi.org/10.1038/nrm2233.
4. Hayflick, L. (1965). The limited in vitro lifetime of human diploid cell strains. Exp. Cell Res. *37*, 614–636. https://doi.org/10.1016/0014-4827(65)90211-9.
5. Borghesan, M., Hoogaars, W.M.H., Varela-Eirin, M., Talma, N., and Demaria, M. (2020). A senescence-centric view of aging: implications for

(F) Causes of death of aging-NC (n = 80; 40 males, 40 females) and aging-302b (n = 80; 40 males, 40 females) mice.
(G) GSEA of multiple tissues in aging-NC vs. aging-302b mice and aging-NC vs. young mice (n = 3 per group). Aging, aging-NC; 302b, aging-302b; young, 12 months old.
Data are shown as means ± SEM. Significance was determined by two-way ANOVA test (B and D), log rank (Mantel-Cox) test (C), or Mann-Whitney U test (E). $^{**}p < 0.01$, $^{***}p < 0.001$. n.s., no significant.

longevity and disease. Trends Cell Biol. *30*, 777–791. https://doi.org/10.1016/j.tcb.2020.07.002.

6. Di Micco, R., Krizhanovsky, V., Baker, D., and d'Adda di Fagagna, F. (2021). Cellular senescence in ageing: from mechanisms to therapeutic opportunities. Nat. Rev. Mol. Cell Biol. *22*, 75–95. https://doi.org/10.1038/s41580-020-00314-w.

7. Gasek, N.S., Kuchel, G.A., Kirkland, J.L., and Xu, M. (2021). Strategies for targeting senescent cells in human disease. Nat Aging *1*, 870–879. https://doi.org/10.1038/s43587-021-00121-8.

8. Huang, W., Hickson, L.J., Eirin, A., Kirkland, J.L., and Lerman, L.O. (2022). Cellular senescence: the good, the bad and the unknown. Nat. Rev. Nephrol. *18*, 611–627. https://doi.org/10.1038/s41581-022-00601-z.

9. Zhang, L., Pitcher, L.E., Yousefzadeh, M.J., Niedernhofer, L.J., Robbins, P.D., and Zhu, Y. (2022). Cellular senescence: a key therapeutic target in aging and diseases. J. Clin. Invest. *132*, e158450. https://doi.org/10.1172/JCI158450.

10. Chaib, S., Tchkonia, T., and Kirkland, J.L. (2022). Cellular senescence and senolytics: the path to the clinic. Nat. Med. *28*, 1556–1568. https://doi.org/10.1038/s41591-022-01923-y.

11. Herranz, N., Gallage, S., Mellone, M., Wuestefeld, T., Klotz, S., Hanley, C.J., Raguz, S., Acosta, J.C., Innes, A.J., Banito, A., et al. (2015). mTOR regulates MAPKAPK2 translation to control the senescence-associated secretory phenotype. Nat. Cell Biol. *17*, 1205–1217. https://doi.org/10.1038/ncb3225.

12. Ocampo, A., Reddy, P., Martinez-Redondo, P., Platero-Luengo, A., Hatanaka, F., Hishida, T., Li, M., Lam, D., Kurita, M., Beyret, E., et al. (2016). In vivo amelioration of age-associated hallmarks by partial reprogramming. Cell *167*, 1719–1733.e12. https://doi.org/10.1016/j.cell.2016.11.052.

13. Childs, B.G., Gluscevic, M., Baker, D.J., Laberge, R.M., Marquess, D., Dananberg, J., and van Deursen, J.M. (2017). Senescent cells: an emerging target for diseases of ageing. Nat. Rev. Drug Discov. *16*, 718–735. https://doi.org/10.1038/nrd.2017.116.

14. Li, Y., Zhao, H., Huang, X., Tang, J., Zhang, S., Li, Y., Liu, X., He, L., Ju, Z., Lui, K.O., et al. (2018). Embryonic senescent cells re-enter cell cycle and contribute to tissues after birth. Cell Res. *28*, 775–778. https://doi.org/10.1038/s41422-018-0050-6.

15. Bi, Y., Qiao, X., Liu, Q., Song, S., Zhu, K., Qiu, X., Zhang, X., Jia, C., Wang, H., Yang, Z., et al. (2022). Systemic proteomics and miRNA profile analysis of exosomes derived from human pluripotent stem cells. Stem Cell Res. Ther. *13*, 449. https://doi.org/10.1186/s13287-022-03142-1.

16. Gong, L., Chen, B., Zhang, J., Sun, Y., Yuan, J., Niu, X., Hu, G., Chen, Y., Xie, Z., Deng, Z., et al. (2020). Human ESC-sEVs alleviate age-related bone loss by rejuvenating senescent bone marrow-derived mesenchymal stem cells. J. Extracell. Vesicles *9*, 1800971. https://doi.org/10.1080/20013078.2020.1800971.

17. Hu, G., Xia, Y., Chen, B., Zhang, J., Gong, L., Chen, Y., Li, Q., Wang, Y., and Deng, Z. (2021). ESC-sEVs rejuvenate aging hippocampal NSCs by transferring SMADs to regulate the MYT1-Egln3-Sirt1 axis. Mol. Ther. *29*, 103–120. https://doi.org/10.1016/j.ymthe.2020.09.037.

18. D'Acunzo, P., Kim, Y., Ungania, J.M., Pérez-González, R., Goulbourne, C.N., and Levy, E. (2022). Isolation of mitochondria-derived mitovesicles and subpopulations of microvesicles and exosomes from brain tissues. Nat. Protoc. *17*, 2517–2549. https://doi.org/10.1038/s41596-022-00719-1.

19. Kugeratski, F.G., Hodge, K., Lilla, S., McAndrews, K.M., Zhou, X., Hwang, R.F., Zanivan, S., and Kalluri, R. (2021). Quantitative proteomics identifies the core proteome of exosomes with syntenin-1 as the highest abundant protein and a putative universal biomarker. Nat. Cell Biol. *23*, 631–641. https://doi.org/10.1038/s41556-021-00693-y.

20. Shay, J.W., and Wright, W.E. (2000). Hayflick, his limit, and cellular ageing. Nat. Rev. Mol. Cell Biol. *1*, 72–76. https://doi.org/10.1038/35036093.

21. Casella, G., Munk, R., Kim, K.M., Piao, Y., De, S., Abdelmohsen, K., and Gorospe, M. (2019). Transcriptome signature of cellular senescence. Nucleic Acids Res. *47*, 7294–7305. https://doi.org/10.1093/nar/gkz555.

22. Wang, S.C., Nakajima, Y., Yu, Y.L., Xia, W., Chen, C.T., Yang, C.C., McIntush, E.W., Li, L.Y., Hawke, D.H., Kobayashi, R., et al. (2006). Tyrosine phosphorylation controls PCNA function through protein stability. Nat. Cell Biol. *8*, 1359–1368. https://doi.org/10.1038/ncb1501.

23. Kaiser, A.M., Gatto, A., Hanson, K.J., Zhao, R.L., Raj, N., Ozawa, M.G., Seoane, J.A., Bieging-Rolett, K.T., Wang, M., Li, I., et al. (2023). p53 governs an AT1 differentiation programme in lung cancer suppression. Nature *619*, 851–859. https://doi.org/10.1038/s41586-023-06253-8.

24. Mahdessian, D., Cesnik, A.J., Gnann, C., Danielsson, F., Stenström, L., Arif, M., Zhang, C., Le, T., Johansson, F., Schutten, R., et al. (2021). Spatiotemporal dissection of the cell cycle with single-cell proteogenomics. Nature *590*, 649–654. https://doi.org/10.1038/s41586-021-03232-9.

25. Ma, S., Wang, S., Ye, Y., Ren, J., Chen, R., Li, W., Li, J., Zhao, L., Zhao, Q., Sun, G., et al. (2022). Heterochronic parabiosis induces stem cell revitalization and systemic rejuvenation across aged tissues. Cell Stem Cell *29*, 990–1005.e10. https://doi.org/10.1016/j.stem.2022.04.017.

26. Ashraf, H.M., Fernandez, B., and Spencer, S.L. (2023). The intensities of canonical senescence biomarkers integrate the duration of cell-cycle withdrawal. Nat. Commun. *14*, 4527. https://doi.org/10.1038/s41467-023-40132-0.

27. Smit, M.A., and Peeper, D.S. (2008). Deregulating EMT and senescence: double impact by a single twist. Cancer Cell *14*, 5–7. https://doi.org/10.1016/j.ccr.2008.06.012.

28. Li, X., Li, C., Zhang, W., Wang, Y., Qian, P., and Huang, H. (2023). Inflammation and aging: signaling pathways and intervention therapies. Signal Transduct. Target. Ther. *8*, 239. https://doi.org/10.1038/s41392-023-01502-8.

29. Tabula; Muris Consortium (2020). A single-cell transcriptomic atlas characterizes ageing tissues in the mouse. Nature *583*, 590–595. https://doi.org/10.1038/s41586-020-2496-1.

30. Ramachandran, P., Dobie, R., Wilson-Kanamori, J.R., Dora, E.F., Henderson, B.E.P., Luu, N.T., Portman, J.R., Matchett, K.P., Brice, M., Marwick, J.A., et al. (2019). Resolving the fibrotic niche of human liver cirrhosis at single-cell level. Nature *575*, 512–518. https://doi.org/10.1038/s41586-019-1631-3.

31. Lake, B.B., Menon, R., Winfree, S., Hu, Q., Melo Ferreira, R., Kalhor, K., Barwinska, D., Otto, E.A., Ferkowicz, M., Diep, D., et al. (2023). An atlas of healthy and injured cell states and niches in the human kidney. Nature *619*, 585–594. https://doi.org/10.1038/s41586-023-05769-3.

32. Belinky, F., Nativ, N., Stelzer, G., Zimmerman, S., Iny Stein, T., Safran, M., and Lancet, D. (2015). PathCards: multi-source consolidation of human biological pathways. Database (Oxford) *2015*, bav006. https://doi.org/10.1093/database/bav006.

33. Ma, S., Sun, S., Geng, L., Song, M., Wang, W., Ye, Y., Ji, Q., Zou, Z., Wang, S., He, X., et al. (2020). Caloric restriction reprograms the single-cell transcriptional landscape of Rattus norvegicus aging. Cell *180*, 984–1001.e22. https://doi.org/10.1016/j.cell.2020.02.008.

34. Subramanyam, D., Lamouille, S., Judson, R.L., Liu, J.Y., Bucay, N., Derynck, R., and Blelloch, R. (2011). Multiple targets of miR-302 and miR-372 promote reprogramming of human fibroblasts to induced pluripotent stem cells. Nat. Biotechnol. *29*, 443–448. https://doi.org/10.1038/nbt.1862.

35. Parchem, R.J., Ye, J., Judson, R.L., LaRussa, M.F., Krishnakumar, R., Blelloch, A., Oldham, M.C., and Blelloch, R. (2014). Two miRNA clusters reveal alternative paths in late-stage reprogramming. Cell Stem Cell *14*, 617–631. https://doi.org/10.1016/j.stem.2014.01.021.

36. Cai, Z., Cao, C., Ji, L., Ye, R., Wang, D., Xia, C., Wang, S., Du, Z., Hu, N., Yu, X., et al. (2020). RIC-seq for global in situ profiling of RNA-RNA spatial interactions. Nature *582*, 432–437. https://doi.org/10.1038/s41586-020-2249-1.

37. Seeley, J.J., Baker, R.G., Mohamed, G., Bruns, T., Hayden, M.S., Deshmukh, S.D., Freedberg, D.E., and Ghosh, S. (2018). Induction of innate immune memory via microRNA targeting of chromatin remodelling factors. Nature *559*, 114–119. https://doi.org/10.1038/s41586-018-0253-5.

38. Kumar, R.M., Cahan, P., Shalek, A.K., Satija, R., DaleyKeyser, A., Li, H., Zhang, J., Pardee, K., Gennert, D., Trombetta, J.J., et al. (2014). Deconstructing transcriptional heterogeneity in pluripotent stem cells. Nature *516*, 56–61. https://doi.org/10.1038/nature13920.

39. Tomasetti, C., Poling, J., Roberts, N.J., London, N.R., Jr., Pittman, M.E., Haffner, M.C., Rizzo, A., Baras, A., Karim, B., Kim, A., et al. (2019). Cell division rates decrease with age, providing a potential explanation for the age-dependent deceleration in cancer incidence. Proc. Natl. Acad. Sci. USA *116*, 20482–20488. https://doi.org/10.1073/pnas.1905722116.

40. Choudhury, A.R., Ju, Z., Djojosubroto, M.W., Schienke, A., Lechel, A., Schaetzlein, S., Jiang, H., Stepczynska, A., Wang, C., Buer, J., et al. (2007). Cdkn1a deletion improves stem cell function and lifespan of mice with dysfunctional telomeres without accelerating cancer formation. Nat. Genet. *39*, 99–105. https://doi.org/10.1038/ng1937.

41. Anders, L., Ke, N., Hydbring, P., Choi, Y.J., Widlund, H.R., Chick, J.M., Zhai, H., Vidal, M., Gygi, S.P., Braun, P., et al. (2011). A systematic screen for CDK4/6 substrates links FOXM1 phosphorylation to senescence suppression in cancer cells. Cancer Cell *20*, 620–634. https://doi.org/10.1016/j.ccr.2011.10.001.

42. Hsu, C.H., Altschuler, S.J., and Wu, L.F. (2019). Patterns of early p21 dynamics determine proliferation-senescence cell fate after chemotherapy. Cell *178*, 361–373.e12. https://doi.org/10.1016/j.cell.2019.05.041.

43. Chang, H.M., and Gregory, R.I. (2011). MicroRNAs and reprogramming. Nat. Biotechnol. *29*, 499–500. https://doi.org/10.1038/nbt.1889.

44. Lapasset, L., Milhavet, O., Prieur, A., Besnard, E., Babled, A., Aït-Hamou, N., Leschik, J., Pellestor, F., Ramirez, J.M., De Vos, J., et al. (2011). Rejuvenating senescent and centenarian human cells by reprogramming through the pluripotent state. Genes Dev. *25*, 2248–2253. https://doi.org/10.1101/gad.173922.111.

45. Stewart-Ornstein, J., and Lahav, G. (2016). Dynamics of CDKN1A in single cells defined by an endogenous fluorescent tagging toolkit. Cell Rep. *14*, 1800–1811. https://doi.org/10.1016/j.celrep.2016.01.045.

46. Mourgues, L., Imbert, V., Nebout, M., Colosetti, P., Neffati, Z., Lagadec, P., Verhoeyen, E., Peng, C., Duprez, E., Legros, L., et al. (2015). The BMI1 polycomb protein represses cyclin G2-induced autophagy to support proliferation in chronic myeloid leukemia cells. Leukemia *29*, 1993–2002. https://doi.org/10.1038/leu.2015.112.

47. Keshavarz, M., Xie, K., Schaaf, K., Bano, D., and Ehninger, D. (2023). Targeting the "hallmarks of aging" to slow aging and treat age-related disease: fact or fiction? Mol. Psychiatry *28*, 242–255. https://doi.org/10.1038/s41380-022-01680-x.

48. Mannick, J.B., Morris, M., Hockey, H.P., Roma, G., Beibel, M., Kulmatycki, K., Watkins, M., Shavlakadze, T., Zhou, W., Quinn, D., et al. (2018). TORC1 inhibition enhances immune function and reduces infections in the elderly. Sci. Transl. Med. *10*, eaaq1564. https://doi.org/10.1126/scitranslmed.aaq1564.

49. Neff, F., Flores-Dominguez, D., Ryan, D.P., Horsch, M., Schröder, S., Adler, T., Afonso, L.C., Aguilar-Pimentel, J.A., Becker, L., Garrett, L., et al. (2013). Rapamycin extends murine lifespan but has limited effects on aging. J. Clin. Invest. *123*, 3272–3291. https://doi.org/10.1172/JCI67674.

50. Wang, B., Wang, L., Gasek, N.S., Kuo, C.L., Nie, J., Kim, T., Yan, P., Zhu, J., Torrance, B.L., Zhou, Y., et al. (2024). Intermittent clearance of p21-highly-expressing cells extends lifespan and confers sustained benefits to health and physical function. Cell Metab. *36*, 1795–1805.e6. https://doi.org/10.1016/j.cmet.2024.07.006.

51. Guo, J., Zhao, H., Zhang, J., Lv, X., Zhang, S., Su, R., Zheng, W., Dai, J., Meng, F., Gong, F., et al. (2023). Selective translation of maternal mRNA by eIF4E1B controls oocyte to embryo transition. Adv. Sci. (Weinh) *10*, e2205500. https://doi.org/10.1002/advs.202205500.

52. El-Andaloussi, S., Lee, Y., Lakhal-Littleton, S., Li, J., Seow, Y., Gardiner, C., Alvarez-Erviti, L., Sargent, I.L., and Wood, M.J.A. (2012). Exosome-mediated delivery of siRNA in vitro and in vivo. Nat. Protoc. *7*, 2112–2126. https://doi.org/10.1038/nprot.2012.131.

53. Xue, Y., Zhou, Y., Wu, T., Zhu, T., Ji, X., Kwon, Y.S., Zhang, C., Yeo, G., Black, D.L., Sun, H., et al. (2009). Genome-wide analysis of PTB-RNA interactions reveals a strategy used by the general splicing repressor to modulate exon inclusion or skipping. Mol. Cell *36*, 996–1006. https://doi.org/10.1016/j.molcel.2009.12.003.

54. Vorhees, C.V., and Williams, M.T. (2006). Morris water maze: procedures for assessing spatial and related forms of learning and memory. Nat. Protoc. *1*, 848–858. https://doi.org/10.1038/nprot.2006.116.

55. Bellantuono, I., de Cabo, R., Ehninger, D., Di Germanio, C., Lawrie, A., Miller, J., Mitchell, S.J., Navas-Enamorado, I., Potter, P.K., Tchkonia, T., et al. (2020). A toolbox for the longitudinal assessment of healthspan in aging mice. Nat. Protoc. *15*, 540–574. https://doi.org/10.1038/s41596-019-0256-1.

56. Liang, S., Wang, F., Han, J., and Chen, K. (2020). Latent periodic process inference from single-cell RNA-seq data. Nat. Commun. *11*, 1441. https://doi.org/10.1038/s41467-020-15295-9.

57. Qiu, X., Mao, Q., Tang, Y., Wang, L., Chawla, R., Pliner, H.A., and Trapnell, C. (2017). Reversed graph embedding resolves complex single-cell trajectories. Nat. Methods *14*, 979–982. https://doi.org/10.1038/nmeth.4402.

58. Zhou, Y., Zhou, B., Pache, L., Chang, M., Khodabakhshi, A.H., Tanaseichuk, O., Benner, C., and Chanda, S.K. (2019). Metascape provides a biologist-oriented resource for the analysis of systems-level datasets. Nat. Commun. *10*, 1523. https://doi.org/10.1038/s41467-019-09234-6.

STAR★METHODS

KEY RESOURCES TABLE

REAGENT or RESOURCES	SOURCE	IDENTIFIER
Antibodies		
anti-p21 Waf1/Cip1 recombinant (12D1E1)	Cell Signaling	Cat# 2947; RRID: AB_823586
Anti-p21 Waf1/Cip1 Monoclonal (F-5)	Santa Cruz Biotechnology	Cat# sc-6246; RRID: AB_628073
anti-p16 INK4A	Abcam	Cat# ab189034; RRID: AB_2737282
anti-Ccng2	Invitrogen	Cat# PA5-100707; RRID: AB_2850211
anti-GAPDH	Abcam	Cat# ab9485; RRID: AB_307275
anti-Alix	Abcam	Cat# ab275377; RRID: AB_3644262
anti-CD63	Abcam	Cat# ab134045; RRID: AB_2800495
anti-TSG101	Abcam	Cat# ab125011; RRID: AB_10974262
anti-Calnexin	Abcam	Cat# ab22595; RRID: AB_2069006
anti-Ki67	Abcam	Cat# ab16667; RRID: AB_302459
anti-Ago2	Abcam	Cat# ab186733; RRID: AB_2713978
anti-γ-H2AX	Cell Signaling	Cat# 9718; RRID: AB_647828
anti-H3K9me3	Abcam	Cat# ab8898; RRID: AB_306848
HRP anti-rabbit IgG	Cell Signaling	Cat# 7074; RRID: AB_2099233
HRP anti-mouse IgG	Cell Signaling	Cat# 7076; RRID: AB_330924
anti-Rabbit IgG H&L (Alexa Fluor® 594)	Abcam	Cat# ab150080; RRID: AB_2650602
anti-Rabbit IgG H&L (Alexa Fluor® 488)	Abcam	Cat# ab15008; RRID: AB_301569
Chemicals, peptides, and recombinant proteins		
Doxorubicin	Sigma	Cat# 25316-40-9
Fetal bovine serum	Gibco	Cat# 10091-148
ncTarget Medium	Nuwacell Biotechnologies Co., Ltd.	Cat# RP01020
DAPI	ThermoFisher	Cat# D1306
EDTA	ThermoFisher	Cat# AM9261
DMEM	ThermoFisher	Cat# 11965092
Xho I	New England Biolabs	Cat# R0146S
Not I	New England Biolabs	Cat# R0189S
TRIzol	Vazyme	Cat# R401-01
FuGENE® HD	Promega	Cat# E2311
Lipofectamine 2000	Life Technology	Cat# 11668019
Protease inhibitor cocktail	Cell Signaling	Cat# 5871
Collagenase I	Sigma	Cat# SCR103
Collagenase IV	Sigma	Cat# C4-BIOC
Dispase	Sigma	Cat# D4693
Red blood cell lysis buffer	BD Biosciences	Cat# 555899
Critical commercial assays		
Senescence β-Galactosidase Staining Kit	Cell Signaling	Cat# 9860
Quantibody Mouse TH17 Array 1	RayBiotech	Cat# QAM-TH17-1
miRNeasy® Mini Kit	Qiagen	Cat# 217004
Dual-Luciferase Reporter Assay Kit	Promega	Cat# E1910
Mouse IL-1β ELISA Kit	R&D systems	Cat# MLB00C
Mouse IFN-γ ELISA Kit	R&D systems	Cat# MIF00
Mouse IL-6 ELISA Kit	R&D systems	Cat# M6000B
Mouse TNF-α ELISA Kit	R&D systems	Cat# MTA00B

(*Continued on next page*)

Continued

REAGENT or RESOURCES	SOURCE	IDENTIFIER
Deposited data		
scRNA-seq data	This paper	GEO: GSE247076
Public scRNA-seq data	Almanzar et al.[29]	GEO: GSE132042
Bulk RNA-seq data	Mendeley Data	https://doi.org/10.17632/899tntr9x2.1
Ago2 Clip-seq data	Mendeley Data	https://doi.org/10.17632/899tntr9x2.1
Data S1. Source data	This paper	N/A
Experimental models: Organisms/strains		
C57BL/6J mice	Beijing Vital River Lab	N/A
BALB/c-nu	Beijing Vital River Lab	N/A
Biological samples		
IMR-90	ATCC	Cat# CCL-186
LO2	KCB	Cat# 200511YJ
NCTC1469	ATCC	Cat# CCL-9.1
HEK 293F	ATCC	Cat# CRL-3249
p21-YFP LO2	Our lab	N/A
Oligonucleotides		
CDKN2A (FWD) 5'- CTCGTGCTGATGCTACTGAGGA-3'	OriGene	N/A
CDKN2A (REV); 5'-GGTCGGCGCAGTTGGGCTCC-3'	OriGene	N/A
CDKN1A (FWD); 5'-AGGTGGACCTGGAGACTCTCAG-3'	OriGene	N/A
CDKN1A (REV); 5'-TCCTCTTGGAGAAGATCAGCCG-3'	OriGene	N/A
IL1A (FWD); 5'-TGTATGTGACTGCCCAAGATGAAG-3'	OriGene	N/A
IL1A (REV); 5'-AGAGGAGGTTGGTCTCACTACC-3'	OriGene	N/A
IL11 (FWD); 5'-GGACCACAACCTGGATTCCCTG-3'	OriGene	N/A
IL11 (REV); 5'-AGTAGGTCCGCTCGCAGCCTT-3'	OriGene	N/A
CCL20 (FWD); 5'-AAGTTGTCTGTGTGCGCAAATCC-3'	OriGene	N/A
CCL20 (REV); 5'-CCATTCCAGAAAAGCCACAGTTTT-3'	OriGene	N/A
Software and algorithms		
Image J	NIH	https://imagej.nih.gov/ij/
GraphPad Prism 10	GraphPad	https://www.graphpad.com/
bcl2fastq	Illumina	https://emea.support.illumina.com/
Rnor_6.0 genome	10×Genomics	https://support.10xgenomics.com/
Seurat package	Github	https://github.com/satijalab/seurat/
MSigDB	GSEA	https://www.gsea-msigdb.org/gsea/msigdb/
Monocle 2	Github	https://github.com/cole-trapnell-lab/monocle-release/
Metascape	OmicSoft Corporation	http://metascape.org
FlowJo 10.10	BD	https://www.flowjo.com/

EXPERIMENTAL MODEL AND STUDY PARTICIPANT DETAILS

Mice

Wild-type C57BL/6J mice were purchased from Beijing Vital River Laboratory Animal Technology Co., Ltd. and housed in an SPF-grade facility at Beijing Vital River Laboratory Animal Technology before the experiments. All experimental procedures were approved by the Institutional Animal Care and Use Committee of the Institute of Biophysics.

Treatment plan

Plan A: At the age of 20 months, male mice were randomly divided into Aging-PBS (n = 30) and Aging-Exos (n = 30) groups and transferred to the Institute of Biophysics, Chinese Academy of Sciences, in an SPF-grade facility with individually ventilated cages. Mice in the Aging-Exos group received a weekly tail vein injection of hESC-Exos (2×10^{10} particles in 200 μL PBS), while those in the Aging-PBS group were administered 200 μL PBS via tail vein injection. The 30th month was selected as the test period.

Plan B: At the age of 25 months, male mice that had naturally shed their dorsal fur were selected and randomly assigned to the Aging-302b (n = 20) and Aging-NC (n = 20) groups. Mice in the Aging-302b group received tail vein injections of Exos-302b (2×10^{10} particles in 200 μL PBS) every two weeks, while mice in the Aging-PBS group were administered 200 μL of PBS using the same delivery procedure. The 30th month was selected as the test period.

Plan C: At the age of 20 months, mice were randomly divided into Aging-NC group and Aging-302b groups, with 80 mice in each group (40 males and 40 females per group). Mice in the Aging-302b group received an intravenous injection of Exos-302b (2×10^{10} particles in 200 μL PBS) via the tail vein every two weeks, while those in the Aging-NC group were injected with 200 μL of PBS via the tail vein on the same schedule. The body weight of the mice was recorded weekly until natural death, and a survival curve was analyzed after the death of all mice. Mice that died were immediately collected for postmortem pathological examination.

METHOD DETAILS

Extraction and identification of hESC-Exos

hESCs were cultured in ncTarget medium (Nuwacell Biotechnologies Co., Ltd., RP01020) and grown to ~80% confluency during the logarithmic phase. A total of 350 mL of conditioned medium was collected for exosome purification. hESC-Exos were isolated by sequential centrifugation (300 × g for 10 min, 2,000 × g for 15 min, and 10,000 × g for 30 min) to remove debris, followed by purification using a continuous sucrose gradient (0.8-2.0 M) at 100,000 × g for 16 hours. Fractions with densities ranging from 1.10 to 1.21 g/mL were pooled, ultracentrifuged again at 100,000 × g for 2 hours, and resuspended in PBS. Exosome characterization was carried out using transmission electron microscopy, nanoparticle tracking analysis, and western blotting for exosomal markers (ALIX, CD63, TSG101), along with Calnexin.[18,19]

Population doubling assays

Cells were passaged every 3 d, with each 6-cm dish receiving 100,000 cells. Cells were counted using an automatic cell counter (Countess 3; Thermo Fisher Scientific) at each passage. Population doubling levels (PDLs) were calculated using the formula: $PD = \log(Nf/N0)/\log_2$, where Nf represents the final cell count and N0 is the initial cell count. The cumulative PDLs were determined by summing the PDLs for each passage. Data are presented as cumulative PDL derived from three independent experiments.

p21-YFP cell line generation

The donor NDA plasmid was generated by assembling the Venus-P2A-Neo plasmid (a gift from Jacob Stewart-Ornstein) and the p21 coding sequence flanked by homology arms corresponding to the target genomic region in LO2 cells. A single guide RNA (sgRNA) (5′-GGCTTCCTGTGGGCGGATTA-3′) was integrated into LentiCrispr v2 (Addgene, 52961) to construct the sgRNA and Cas9 expression plasmids. The two plasmids were transfected into LO2 cells to introduce targeted double-stranded breaks at predetermined sites within the genome using FuGENE® HD (Promega, E2311). Following transfection for 4 d, the cells were subjected to selection pressure using geneticin at 500 μg/mL in a selective medium for 7 d. Clones with successful integration of the p21-YFP gene were obtained by limiting dilution, subsequently verified using genomic PCR, and termed p21-YFP LO2 cells.

Preparation of doxorubicin-induced SnCs

We established a cellular senescence model using the following approach: well-grown p21-YFP LO2 cells were treated with stress medium (complete medium containing 50 nM Dox) for 48 h, cultured in normal growth medium for 10 d, and the medium was changed every 2 d. Single SnCs were sorted via flow cytometry (FACSCalibur, BD Biosciences) based on p21 expression.

Cell cycle analysis

Cells were harvested and washed with PBS thrice, followed by fixation with ice-cold 75% ethanol overnight at 4 °C, and washed with PBS twice. Cells (1×10^6) were stained with PI staining buffer (50 μg/mL) in the dark for 30 min at 37 °C and analyzed using a flow cytometer.

Live-cell workstation observation

The p21-YFP positive LO2 cells were plated in a 4-chamber 35 mm Glass bottom dish (Cellvis) and cultured in phenol red-free DMEM supplemented with 10% FBS. The cells were exposed to either PBS or hESC-Exo treatment in an incubator set at 37 °C temperature and 5% CO_2, and subsequently, the long-term live-cell imaging record was completed using a Zeiss LSM980 with Airyscan2 equipped with a 20X objective (Zeiss, N010098).

In vivo safety assessment of hESC-Exos

To evaluate the tumorigenicity of hESC-Exos, 6- to 8-week-old BALB/c nude mice were divided into two groups (n = 10 per group). The experimental group received weekly subcutaneous injections of hESC-Exos (2×10^{10} particles in 200 μL PBS) in the axillary region. The control group was injected with HeLa cells (1×10^6 cells in 200 μL PBS) as a positive control. Tumor size in the HeLa group was measured weekly with a digital caliper, and volume was calculated as $(\text{length} \times \text{width}^2)/2$. Mice were euthanized if tumor volume reached 1,500 mm^3 or observed until week 40 if this limit was not exceeded. The hESC-Exos group was monitored weekly for tumor formation up to week 40. At the endpoint, tissues from the injection site were collected for histological analysis.

Urine spot assay

Mice were placed in a carton covered with a layer of A4 paper. After 3 h of unrestricted movement, the A4 paper was removed, dried, and photographed under ultraviolet (UV) light. Subsequently, the count of urinary spots was quantified using the ImageJ software.

Immunofluorescence microscopy

Fresh tissue was embedded in OCT and rapidly frozen, then sectioned into 10 μm-thick slices using a cryo-microtome (Leica CM1950). Alternatively, cells were seeded on coverslips for 2 days before staining. Slides were washed with PBS, fixed with 4% paraformaldehyde (PFA) for 30 min, and permeabilized with 0.5% Triton™ X-100 (ThermoFisher, 85111) for 20 min. After blocking with 10% goat serum in PBS for 1 h, slides were incubated overnight at 4°C with primary antibodies, followed by 1-hour incubation at 37°C with fluorescence-labeled secondary antibodies. After three 5-minute PBS washes, nuclei were counterstained with DAPI. Images were captured using a Leica SP5 confocal microscope.

Postmortem pathological examination

Carcasses were collected within 12 hours and individually fixed into 10% formaldehyde. After the gross pathological examination, tissues were embedded in paraffin and stained with hematoxylin-eosin. After examination of both neoplastic and non-neoplastic diseases, tumor burden (the sum of tumors per mouse) and disease burden (the sum of histopathological alterations per mouse) were evaluated as previously described.[50]

Bulk RNA-seq

RNA data were processed as previously described.[51] The total RNA was converted to cDNA and sequenced. After quality control and adaptor trimming, the sequencing reads were aligned to the UCSC human hg19 genome using the HISAT2 software (version 2.2.0) (https://daehwankimlab.github.io/hisat2/). Differentially expressed genes were identified through the application of DESeq2 (version 1.41.8) employing a threshold based on a Benjamini-Hochberg adjusted p-value of 0.05 and an absolute fold change of > 2 (|Log2FC| >1). Identified DEGs were mapped to GO terms to determine their biological and functional properties.

SA-β-gal staining

SA-β-gal staining was performed as described previously.[33] The OCT-embedded, snap-frozen, unfixed tissues were cryosectioned at a thickness of 10 μm using the Leica CM1950 cryo-microtome. Sections were collected on Superfrost Plus microslides and stored at -80 °C until use. For SA-β-gal staining, the sections were thawed and washed in 1×PBS, fixed with a combination of 2% formaldehyde and 0.2% glutaraldehyde at 37 °C for 5 min, and stained with a freshly prepared staining solution (X-gal, Sigma) at 37 °C overnight. Micrographs were acquired using a panoramic scanning instrument (Leica CS2), and the percentage of positive regions was quantified using the ImageJ software. Cellular samples were subjected to SA-β-gal staining following the procedure described above.

Cytokine array assay of mice serums

The serum protein extracts were diluted to 500 mg/mL in blocking buffer and incubated overnight with the corresponding anti-cytokine antibodies on the antibody arrays (RayBiotech, QAM-TH17-1). After washing, biotin-conjugated anti-cytokine antibodies were incubated for 2 hours, followed by incubation with Cy3-conjugated streptavidin for glass arrays or HRP-conjugated streptavidin for membrane arrays for 2 hours. Fluorescent signals were detected using an InnoScan 300 Microarray Scanner (Innopsys, France), and chemiluminescent signals were captured with an ImageQuant LAS4000 Scanner (GE Healthcare, USA). Data were normalized using an internal positive control and analyzed with RayBiotech's analysis tool.

Absolute quantification of miR-302b by RT-qPCR

Standard miR-302b samples were synthesized by GenePharma Co. Ltd. (Suzhou, China). A standard curve was generated by preparing seven 10-fold serial dilutions starting from 1 μM miR-302b mimics. cDNA was synthesized using the miRNA First-Strand Synthesis Kit (Takara, 638313) and analyzed by RT-qPCR with SYBR Green PCR Master Mix (Solarbio, SR1120) on a Rotor-Gene-Q instrument (Qiagen, Hilden, Germany). The standard curve, correlating copy number and miRNA concentration, was used for subsequent quantification. Total RNA was extracted from fresh tissues or cells using the miRNeasy® Mini Kit (Qiagen, 217004), quantified with Nanodrop, and the A260/A280 ratio was assessed. miR-302b concentration was determined via RT-qPCR using the standard curve, with all reactions performed in triplicate.

Preparation of exosomes loaded with miR-302b mimics

The culture supernatant was collected from the suspended 293F cells to extract exosomes, termed 293F-Exos, which were subsequently identified. For electroporation, miR-302b mimics (GenePharma, China) were mixed with 293F-Exos in a 1:1 (w/w) electroporation buffer, as described previously.[52] The mixture was loaded into the Neon Tip and subjected to electroporation at 0.5 kV, employing a 10-ms pulse for 5 min using the Neon Transfection System, according to the manufacturer's instructions (Thermo Fisher Scientific). The miR-302b in prepared exosomes, namely Exos-302b, was quantified using absolute quantitative real-time qPCR.

Luciferase assays

Luciferase reporters were meticulously constructed by integrating Ago2-bound fragments into the psiCHECK-2 vector positioned between the *Xho* I and *Not* I restriction sites.[36] Cells were seeded into 24-well plates and transfected with a mixture comprising 25 ng of reporter plasmid and 40 pmol of the miR-302b mimic using Lipofectamine 2000 (Life Technology, 11668019). Luciferase activity was quantified using a Dual-Luciferase Reporter Assay Kit (Promega, E1910) on a Veritas Microplate Luminometer (Promega).

Ago2 Clip-seq

IMR-90 cells transfected with miR-302b mimics were subjected to ultraviolet irradiation at 254 mJ and harvested by scraping the cells from 15-cm plates. Ago2 Clip-seq was performed as previously described.[36,53] The cell lysate was immunoprecipitated using an anti-Ago2 antibody (Abcam, ab186733) to enrich the Ago2 protein and its binding RNAs. Immunoprecipitated RNA was extracted using TRIzol reagent, and after DNase I treatment, the purified RNA was reverse transcribed to synthesize cDNA for subsequent high-throughput sequencing. Based on the sequence alignment analysis, prospective binding sites for miR-302b were identified.

Mirror water maze

Mice were trained to navigate a circular water maze (120 cm diameter, 30 cm height) and find a hidden platform using room cues. The pool was filled with opaque water at 24.0 ± 0.5 °C and divided into four quadrants. Mice underwent 3 days of cued training, 5 days of acquisition training, and a final probe trial. In cued training, a triangular flag marked the platform, and mice were given 1 min to locate it. Mice failing to find the platform were guided to it for 10 s. During acquisition training, the flag was removed, and visual cues were placed around the pool. After 48 hours, a probe trial was conducted by removing the platform and introducing mice from a novel entry point. Mice swam for 1 min, and escape latency and quadrant preference were tracked using a video tracking system (Ethovision Noldus, Netherlands).[54]

Grip strength test

The grip strength test was performed as previously reported.[55] A grip strength meter (Ugo-Basile, Italy) was used to measure the forelimb muscle strength. The grip strength meter was arranged horizontally on the table, and the mice could grip the trapezius or grid using both the forehand and hind paws, while the experimenter held their tail. The mice were gently drawn backward until their grip was relinquished. The peak force for each measurement was automatically recorded using a meter. The test was performed in five independent replicates, and the data were normalized to the body weight of the mice.

Rotarod test

The rotarod test was used to assess motor coordination and balance in rodents. Mice were acclimatized for 3 days before testing. On Day 1, the exercise duration was 5 min, with a maximum rotational speed of 20 rpm, and a uniform acceleration duration of 300 s. On Day 2, the exercise duration remained at 5 min, but the maximum rotational speed increased to 40 rpm, with the uniform acceleration duration of 300 s. The third day's exercise duration extended to 8 min, with a maximum rotational speed of 60 rpm and uniform acceleration for 300 s. The fourth day's exercise duration lasted 10-min, with the maximum rotational speed reaching 80 rpm, and the acceleration duration remained at 300 s. Additionally, on the first day, mice underwent a rotarod test at a fixed speed of 25 rpm.[55]

Statistical analysis of scRNA-seq data

scRNA-seq was performed using the 10 × platform (Bestopcell, Beijing). Sequencing data were processed with bcl2fastq for demultiplexing and aligned to the Rnor_6.0 genome to create a pre-mRNA reference. Gene counts were computed with Cell Ranger and used to generate a filtered count matrix for analysis. Data were analyzed with Seurat (version 4.9.9) for filtering, normalization, dimensionality reduction, clustering, and differential expression. Cell types were assigned based on marker genes (Table S2).[33]

Cell cycle genes were defined using Gene Ontology from MSigDB version 3.1. Four cell cycle signatures (G1/S, S, G2/M, M) were calculated and refined by averaging genes with high correlation to phase-specific signatures. Cells were ranked based on their progression along the cycle.[56] Differential expression analysis between groups (Aging-PBS vs. Young and Aging-PBS vs. Aging-Exos) was performed using the Wilcoxon rank-sum test.[33] DEGs with $|Log_2FC| > 1$ and p-value < 0.05 were selected. Rescue DEGs were defined as those overlapping between Aging and Exos DEGs. Pseudo-time analysis was performed with Monocle 2, using differential expression and dispersion (q-value < 0.1) for gene ordering and visualized in pseudo-time order using DDRTree.[57] GO enrichment and pathway analysis were conducted using Metascape (http://metascape.org) and visualized with ggplot2 (version 3.4.2), with significance set at p-value < 0.01.[58]

QUANTIFICATION AND STATISTICAL ANALYSIS

Log-rank (Mantel-Cox) test was used for survival and median lifespan analysis. Mann-Whitney U test and Fisher's Exact test were used for maximum lifespan analysis. Mixed-effects Cox regression was employed to assess between-group survival differences using hazard ratios for mortality, including a random cage effect and the fixed effects of sex and treatment (Aging-NC vs. Aging-302b). All results are expressed as mean ± SEM. n indicates the number of animals per test group unless otherwise indicated. Statistical

analyses were performed using one-way ANOVA test, two-way ANOVA test, or Student's t-test in PRISM software (GraphPad Prism 10) to compare the differences between the treatment and control groups, assuming equal variance. *, **, and *** indicate $p < 0.05$, $p < 0.01$, and $p < 0.001$, respectively. n.s., no statistically significant difference. All experiments were repeated at least three times.